Acta Astronautica 234 (2025) 368–386

Contents lists available at ScienceDirect

Acta Astronautica

journal homepage: www.elsevier.com/locate/actaastro

Development of a hanging pendulum thrust stand for pulsed plasma thrusters

Yueh-Heng Li [a,b,c,*], Wai-Cheng Lien [b], Sheng-Wen Liu [c]

[a] Institute of Space Systems Engineering, National Cheng Kung University, Tainan, 70101, Taiwan
[b] Department of Aeronautics and Astronautics, National Cheng Kung University, Tainan, 70101, Taiwan
[c] International Doctoral Degree Program on Energy Engineering, National Cheng Kung University, Tainan, 70101, Taiwan

ARTICLE INFO

Keywords:
Thrust stand
Electric propulsion
Pulsed plasma thruster
Impulse measurement methods

ABSTRACT

Thrust stands are essential tools for evaluating the performance of propulsion systems, including Hall effect thrusters, ion thrusters, and pulsed plasma thrusters (PPTs). Our thrust stand supports a prototype weighing up to 0.8 kg and measures impulses from 150 to 550 μN s. It generates voltage oscillations with peaks between 5 mV and 35 mV, which, combined with NI voltage modules, minimizes weight constraints on the propulsion system while maintaining accurate measurements under low thrust-to-weight conditions.

This design introduces a novel approach compared to conventional torsional thrust stands. By aligning the propulsion system's center of mass with the pendulum arm, we eliminate the need for spring torque. Instead, gravitational torque provides the necessary equivalent spring constant for damping. The eddy-current damper, featuring a copper plate, doubles as both a damping mechanism and a counterweight, allowing adjustments for different propulsion system weights. Unlike elastic pivots, this design avoids performance degradation from material fatigue or thermal effects.

Challenges in the current system include non-linear spring and damping coefficients caused by PPT power cables and pulse-width errors during calibration. Future improvements will consist of cable feed-throughs to isolate vibrations without introducing unwanted coefficients. Additionally, the improvement aims to optimize the impulse generator's power supply to eliminate calibration errors caused by high-voltage pulse-width fluctuations.

1. Introduction

Thrust is arguably the most fundamental and critical performance parameter in propulsion systems. However, because most electric propulsion systems operate within a low-thrust range, directly measuring thrust poses significant challenges [1]. A widely used method for measuring thrust in electric propulsion systems is the swing force measurement method, which involves mounting the thruster ona pendulum's arm. When the thruster generates force, the pendulum arm experiences angular displacement. The thruster's thrust can be calculated by analyzing the relationship between the angular displacement and the force outputFigure 13.

The nature of this angular displacement varies depending on the thruster type. For continuous electric propulsion systems, such as Hall effect thrusters (HET) [2] and ion thrusters (IOT) [3–5], the thrust ideally remains constant over time, leading to a steady angular displacement. Conversely, pulsed electric propulsion systems, such as pulsed plasma thrusters (PPT) [6–9] and vacuum arc thrusters (VAT) [10], generate thrust in microsecond bursts. As a result, the pendulum arm undergoes rapid angular motion after each pulse, oscillating around its zero position before settling. For such systems, thrust stands not only measure angular displacement to determine thrust magnitude but also rely on extended oscillation periods to increase measurement time, thereby relaxing the temporal resolution requirements of displacement sensors [11].

Thrust stands can be categorized into three main types based on pendulum design: hanging pendulum [12–19], inverted pendulum [20,21], and torsional pendulum [22–26]. The hanging pendulum design is the most straightforward and stable [12]. The thruster is below the pivot point, with an elastic pivot and gravitational torque providing the restoring force. The inverted pendulum offers the highest measurement sensitivity [1], with the thruster mounted below the pivot. However,

---

[*] Corresponding author. Department of Aeronautics and Astronautics, National Cheng Kung University, Tainan, 701, Taiwan.
E-mail address: yueheng@mail.ncku.edu.tw (Y.-H. Li).

https://doi.org/10.1016/j.actaastro.2025.05.003
Received 10 February 2025; Received in revised form 3 April 2025; Accepted 1 May 2025

this design requires the pivot's elastic properties to stabilize the thruster and counteract toppling, limiting its load capacity and structural stability. The torsional pendulum is unique because angular displacement is independent of the thruster's mass [1]. In this configuration, the pivot-pointing-to-thrust axis is parallel to the ground, and the pivot's rotational axis is vertical.

Compared to the other two designs, the hanging pendulum is better suited to systems where elastic pivots are undesirable due to material fatigue or temperature sensitivity. Instead, the hanging pendulum utilizes the thruster's mass as a source of gravitational torque. Given the requirements of this study's prototype, this research selects the hanging pendulum type.

The first application of the hanging pendulum thrust stand for PPT impulse measurement dates back to 1969 when Radley et al. used a laser and mirror system to measure single-shot impulses [17]. A mirror mounted on the pendulum arm reflected a laser beam onto a ruler 8 feet away. By analyzing the motion of the laser spot, they calculated the initial velocity of the pendulum and, consequently, the impulse of the thruster. In 1999, Lewis et al. refined this system for measuring impulses from miniaturized chemical thruster arrays [14]. They introduced a standardized impulse calibration device, where a metal ball was released down a slope to strike the pendulum arm, generating a known impulse, which allowed them to establish a relationship between impulse and angular displacement. Additionally, they incorporated an eddy-current damper to speed up oscillation decay and improve calibration efficiency.

In 2019, Zhang et al. applied the hanging pendulum thrust stand to measure laser-induced thrust [16]. It replaced the slope-based calibration device with a pendulum-based one, where a hammer released from different angles struck the arm to generate standardized impulses. It added a stress sensor to the hammer's impact surface to ensure accurate measurement. The literature also introduced counterweights to adjust the center of mass and control gravitational torque, enabling precise measurements of single-shot impulses in the micro-Newton-second range.

Among the components of a thrust stand, the calibration device is the most critical. The accuracy and precision of thrust measurements depend entirely on the calibration device. Standard calibration methods include gas dynamics [27,28], piezoelectric impact hammers (PIH) [29,30], and electrostatic combs (ESC) [28,30,31]. Gas dynamics calibration uses controlled exhaust flow rates to generate small momenta, simulating thruster thrust. However, it is sensitive to orifice size and stagnation pressure. ESCs, on the other hand, provide highly repeatable and precise calibration by generating constant electrostatic forces by attracting oppositely charged ions. Although geometric factors and oscillation-induced errors affect ESCs, their simplicity and non-contact design make them ideal for μN- to mN-level calibration. PIH calibration uses a servo-motor-driven hammer to deliver precise impulses, but it is more complex at lower impulse ranges than ESCs. For this study, we selected an ESC for its simplicity and precision.

The subject of this study is the third-generation PPT prototype developed by NCKU ZAPLab. The lab has been developing electric propulsion systems since 2017, including continuous [3,6,32–36] and pulsed [7–10,37] electric propulsion technologies. The first-generation PPT prototype, developed in 2019, used a parallel plate structure with two electrodes, a solid propellant, and an igniter [6]. When ignited, the propellant was vaporized and ionized between the electrodes, generating Lorentz forces to accelerate the ions and produce thrust. While the initial design achieved an impulse of 428.3 μN s per 25 J energy input, subsequent attempts to increase thrust through a segmented electrode structure were less effective, producing only 72.35 μN s under similar conditions [9].

In 2023, the second-generation PPT prototype introduced adjustable electrode lengths and spacing to study their effects on impulse generation [7]. It found that shorter electrodes and higher capacitance yielded more significant impulses, with a maximum impulse of 1.97 μN s achieved at 1 J energy input. However, issues with ion deflection due to electric fields in the parallel-plate structure led to a third-generation design featuring a coaxial electrode configuration. This design focuses ion acceleration along the central axis, achieving a predicted impulse of 340 μN s at 5 J energy input—significantly outperforming existing PPT designs, which typically generate 40–42.86 μN s at the same energy level.

Before measuring the PPT's impulse, the study calibrated ESC and thrust stand. The ESC was tested on an electronic scale to determine the force generated at various voltages. Using the ESC to establish a relationship between impulse and angular displacement, standardized impulses were then applied to the thrust stand. The study calculated the impulse by analyzing the thrust stand's angular response following a PPT firing. The study also assessed the uncertainty of these measurements and their contributing factors.

1.1. Angular displacement of hanging pendulum thrust stand

The hanging pendulum thrust stand consists of two primary components: a static structure and a swinging pendulum. The static structure supports the pendulum above the ground and provides a platform for mounting additional components, as shown in Fig. 1.

The swinging pendulum directly connects to the thruster, converting its firing impulse into an angular response. The fundamental governing equation of motion is expressed as [1]:

$$I\ddot{\theta}+c\dot{\theta}+k\theta=F(t)L_t \tag{1}$$

where.

- I is the inertia of swing pendulum $(kg\cdot m^2)$
- c is the effective damping constant of swing pendulum $\left(Nm\cdot s/_{rad}\right)$
- k is the effective spring constant of swing pendulum $\left(Nm/_{rad}\right)$
- L_t is the distance between impulse center and pivot center (m)
- $F(t)$ is the input force of firing impulse altering with time (N)
- $\theta(t)$ is the angular response of swing pendulum (rad)

Rewritten as:

$$\ddot{\theta}+2\xi\omega_n\dot{\theta}+\omega_n^2\theta=F(t)\frac{L_t}{I} \tag{2}$$

where.

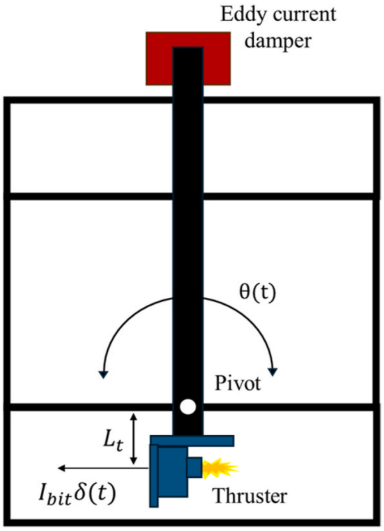

Fig. 1. Schematic of hanging pendulum thrust stand (neglect ESC, eddy current damper, displacement sensor etc.).

- ξ is the damping ratio of swing pendulum

$$\xi = \frac{c}{2}\sqrt{\frac{1}{Ik}} \tag{3}$$

- ω_n is the natural frequency of swing pendulum (Hz):

$$\omega_n = \sqrt{\frac{k}{I}} \tag{4}$$

Although some thrust stand designs incorporate elastic pivots to provide a return-to-zero force, the pendulum in this setup naturally returns to its zero-position due to gravitational torque T_g

$$T_g = mgL_{cm} \sin\theta \cong mgL_{cm}\theta \tag{5}$$

where.

- L_{cm} is the distance between pivot and weight center of swing pendulum and connected thruster (m)
- g is gravitational acceleration (9.81 $m/_{s^2}$)
- m is the total mass of swing pendulum and connected thruster (kg)

For small angular displacements, $\sin\theta$ is approximated as θ. The total effective spring constant k of the pendulum system is given by:

$$k = k_s + \frac{T_g}{\theta} = k_s + mgL_{cm} \tag{6}$$

where k_s is the spring constant of elastic pivots in other thrust stands, as a result, the value is zero in this thrust stand.

When a single impulse is applied, represented by $F(t) = I_{bit}\delta(t)$, where $\delta(t)$ is the Dirac delta function simulating the pulsed force from a PPT, the angular response can be derived. Substituting this into the motion equation gives:

$$\theta(t) = \begin{cases} \frac{I_{bit}L_t}{I\omega_n}\left[\frac{1}{\sqrt{1-\xi^2}}e^{-\xi\omega_n t}\sin(\omega_d t)\right] & \text{if } \xi < 1 \\ \frac{I_{bit}L_t}{I\omega_n}\left[\omega_n t e^{-\omega_n t}\right] & \text{if } \xi = 1 \\ \frac{I_{bit}L_t}{I\omega_n}\left[\frac{1}{2\sqrt{\xi^2-1}}\left(e^{-d_1\omega_n t} - e^{-d_2\omega_n t}\right)\right] & \text{if } \xi > 1 \end{cases} \tag{7}$$

where.

- ω_d is the damped frequency of swing pendulum (Hz):

$$\omega_d = \omega_n\sqrt{1-\xi^2} \tag{8}$$

- $d_1 = \xi - \sqrt{\xi^2 - 1}$ and $d_2 = \xi + \sqrt{\xi^2 - 1}$

The thrust stand in this research operates as an **underdamped system** (Fig. 2), focusing on the case where $\xi < 1$.

The time of maximum angular deflection t_m occur when $\dot{\theta}(t) = 0$, leading to:

$$t_m = \frac{1}{\omega_d}\tan^{-1}\left(\frac{\omega_d}{\xi\omega_n}\right) \tag{9}$$

Substituting t_m back into $\theta(t)$, the maximum angular deflection θ_m becomes:

$$\theta_m = e^{-\frac{\xi}{\sqrt{1-\xi^2}}\tan^{-1}\left(\frac{\sqrt{1-\xi^2}}{\xi}\right)}\frac{L_t}{I\omega_n}\cdot I_{bit} \tag{10}$$

Eq. (10) shows the impulse bit I_{bit} is proportional to the maximum angular deflection θ_m, leading to the thrust stand calibration.

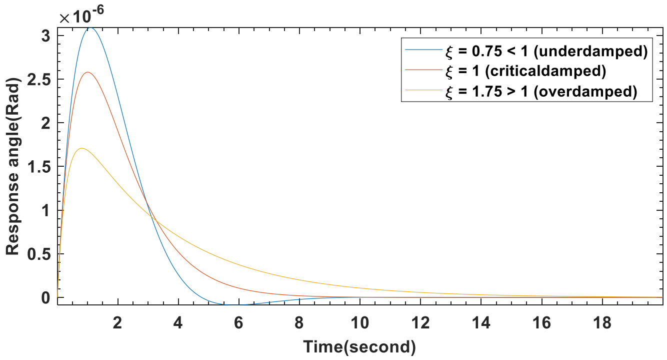

Fig. 2. The angular response of under-, critical-, and overdamped pendulum to a 10 μN s impulse bit ($L_t = 0.77$, $w_n = 0.9964$, $w_d = 0.6591$, and $I = 0.1102$).

1.2. Standard impulse of electrostatic comb (ESC) actuator

The electrostatic comb (ESC) operates by generating an electrostatic force between a fixed electrode (fixed finger) and a movable electrode (movable finger). The movable finger, connected to the thrust stand's pendulum, is grounded, while the fixed finger, part of the thrust stand's frame, is subjected to a high potential difference at the kilovolt level.

The fringing effect influences the electrostatic field between the fingers, causing the field lines to bend near the edges. The field can divided into two components [38].

1. **Local Electrostatic Field**: Exists in the overlapping region of the two fingers.
2. **Global Electrostatic Field**: Extends beyond the engaged region and is influenced by the fringing effect.

Fig. 3 shows the front and top views of a pair of electrostatic fingers. Assuming the fingers overlapping depth x_0 is significantly larger than the geometric dimensions (l_1, l_2, l_3), the fringe field in the engaged region can be approximated as uniform. With the virtual work principle, the local field energy U_{field}^{Local} is expressed as:

$$U_{field}^{Local} = \frac{\varepsilon_0}{2}\iiint_{\mathscr{V}} |\overline{E}|^2 d\mathscr{V} \approx x_0 VQ \tag{11}$$

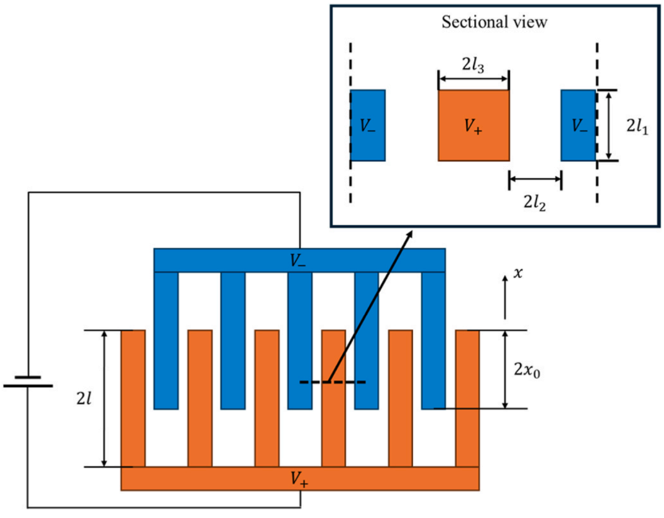

Fig. 3. Schematic of electrostatic comb combined by movable finger and fixed finger plus the sectional view at the middle of the fingers.

where.

- ε_0 is the vacuum permittivity ($8.854 \times 10^{-12} F/_m$).
- $\overline{E}$ is the electric field between electrostatic fingers ($V/_m$)
- $\mathscr{V}$ is the volume of the finger overlapping region (m^3)
- V is the applied voltage between the fingers (V)
- Q is the charge unit depth of each finger (C)

The force per unit length, F_x^{Local}, is derived by differentiating the local field energy U_{field}^{Local} with respect to the engaged length $2x_0$:

$$F_x^{Local} \approx \frac{\delta U^{Local}}{\delta(2x_0)} = \frac{1}{2}\frac{\delta U_{field}^{Local}}{\delta x_0} = \frac{VQ}{2} \tag{12}$$

The charge Q per unit length, based on the ESC geometry, is given by Ref. [38]:

$$Q \cong \varepsilon_0 \frac{2l_1}{l_2} V + 2\varepsilon_0 V K\left[\sin\left(\frac{\pi l_3}{2(l_3+l_2)}\right)\right] \Big/ K\left[\cos\left(\frac{\pi l_3}{2(l_3+l_2)}\right)\right] \tag{13}$$

Here, l_1, l_2, l_3 are geometric dimensions of the ESC, and $K(\eta)$ is the complete elliptic integral of the first kind.

Substituting Eq. (14) into the force equation Eq. (13), the local force becomes:

$$F_x^{Local} \approx \varepsilon_0 V^2 \left\{\frac{l_1}{l_2} + K\left[\sin\left(\frac{\pi l_3}{2(l_3+l_2)}\right)\right] \Big/ K\left[\cos\left(\frac{\pi l_3}{2(l_3+l_2)}\right)\right]\right\} \tag{14}$$

The global force F_x^{Global} due to the free-space currents in these regions is given by:

$$F_x^{Global} = 4(l_2 + l_3)\frac{\varepsilon_0 V^2}{4\pi x_0} \tag{15}$$

Combining the local and global contributions, the total force F_{ESC} generated by the comb is approximate as [39]:

$$F_{ESC} \approx 2N\varepsilon_0 V^2 \left[2.2464 - \frac{(l_2 + l_3)}{\pi x_0}\right] \tag{16}$$

where N is the number of finger pair

Since thrust stand calibration relies on pulsed thrust, the ESC must be applied to pulsed voltage to produce thrust impulses. However, practical challenges arise due to the narrow pulse width (on the order of microseconds) required by pulsed plasma thrusters (PPTs). If the pulse width t_d is shorter than the settling time t_m of the thrust stand, the entire impulse is stored as potential energy in the angular displacement. Under these conditions, the angular response is unaffected by variations in pulse width, provided the total impulse remains constant [1].

The pulse width t_d must satisfy:

$$t_d \le t_s = \frac{4}{\xi \omega_n} \tag{17}$$

where ξ is the damping ratio ($0.4 \le \xi \le 0.8$) and ω_n is the natural frequency of the system.

1.3. Physics of pulsed plasma thruster

Pulsed plasma thrusters (PPTs) are propulsion systems that utilize electromagnetic acceleration to generate thrust. The most classic configuration is the parallel-plate PPT, where the interaction between the magnetic field created during discharge and the current produces Lorentz forces that accelerate charged particles. This mechanism forms the foundation of the PPT's thrust generation.

As shown in Fig. 4, a perpendicular magnetic field $\vec{B}$ is applied toa bridge current $\vec{j}$ induced by parallel electric field,. When charged particles pass through this field, they experience a Lorentz force F_L that accelerates them in a specific direction. Based on this principle, charged particles are expelled to generate thrust [40–42] (see Fig. 5).

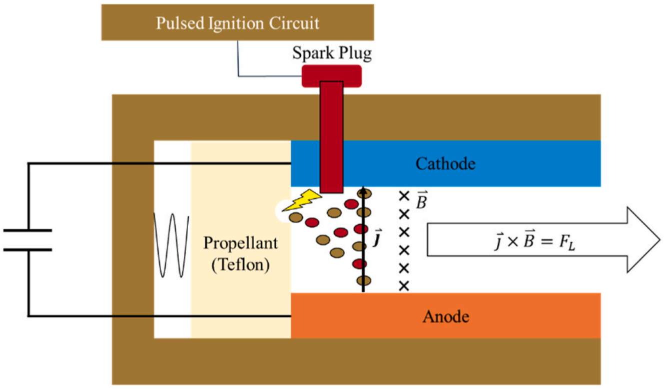

Fig. 4. Schematic of the most classic configuration of pulsed plasma thruster, parallel plate pulsed plasma thruster.

PPT thrust is composed of two main contributions.

1. **Electromagnetic Contribution** (T_{em}): Arising from the Lorentz force due to the interaction of current and magnetic fields.
2. **Electrothermal Contribution** (T_{et}): Resulting from the high temperatures generated during propellant ablation, which create a pressure differential at the nozzle to produce thrust.

The total impulse of the PPT I_{bit} is given by:

$$I_{bit} = \int T_{em} dt + \int T_{et} dt \tag{18}$$

The electromagnetic thrust can be expressed as:

$$T_{em} = \frac{1}{2} L' \int I^2 dt \tag{19}$$

where.

- L' is the inductance gradient, which depends on the geometry of the PPT ($H/_m$).
- I is the discharge current during operation (A).

For different PPT configurations, the inductance gradient L' is defined as follows:

1. Coaxial PPT:

$$L' = \frac{\mu_0}{2\pi}\left[ln \frac{r_a}{r_c} + 0.75\right] \tag{20}$$

- r_a is the radius of the inner electrode (m)
- r_c is the radius of the outer electrode (m)
- μ_0 is the permeability of free space ($4\pi \times 10^{-7} mkg/_{s^2 A^2}$)

2. Parallel-Plate PPT:

$$L' = \frac{\pi}{2}\frac{h}{w} \tag{21}$$

- h is the distance between the electrodes (m)
- w is the electrode width. (m)

Electrothermal thrust arises from the propellant's high-temperature gas expansion. This can be expressed as:

$$T_{et} = \int T_{gas} dt = \iint p dA dt \tag{22}$$

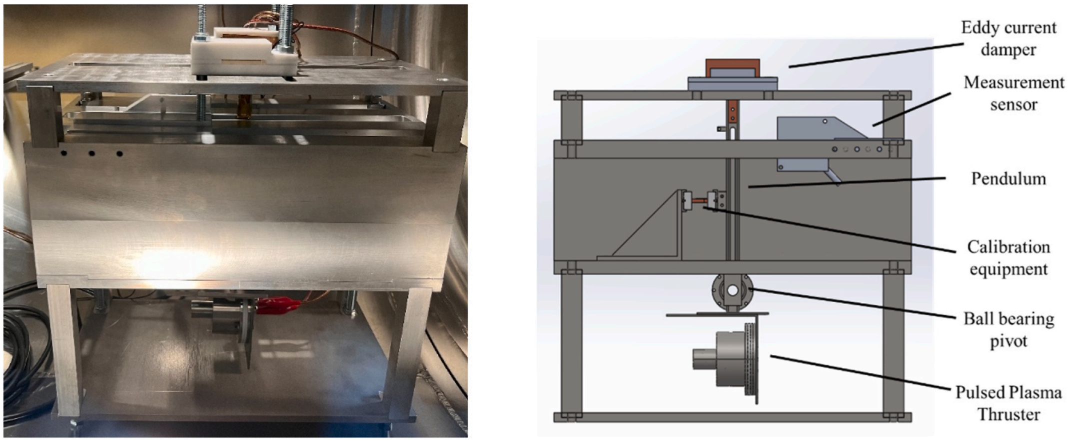

(a) (b)

Fig. 5. Hanging pendulum-type thrust stand designed by ZAPLab (a) Thrust stand inside vacuum chamber (b) Schematic the core components of the stand.

Assuming an adiabatic, constant-volume process, the gas pressure p is related to the stored energy E_0 and the discharge channel's volume $L \times A$:

$$p = (\gamma - 1)\frac{E_0}{LA} \tag{23}$$

Using this, the electrothermal impulse per joule of energy can be approximated as:

$$\frac{\int T_{gas} dt}{J} \cong \frac{pAL/a}{E_0} \cong \frac{\gamma - 1}{a} \tag{24}$$

Combining electromagnetic and electrothermal contributions, the theoretical total impulse I_{bit} of the PPT is:

$$I_{bit} = E_0\left[\frac{L'}{2R} + \frac{\gamma - 1}{a}\right] \tag{25}$$

where.

- E_0 is the storage energy (J)
- R is the circuit resistance (Ω)
- a is the speed of sound (varies with arc temperature) (m/s)
- γ is the specific heat ratio of the propellant.

In practical PPT operation, not all input energy is converted into thrust. Energy losses occur due to Refs. [41,42].

1. **Circuit Resistance:** Energy dissipates as heat within the circuit.
2. **Propellant Ablation:** Energy is consumed to convert solid propellant into plasma.
3. **Joule Heating:** Resistive heating further reduces energy efficiency.

These losses mean that only a fraction of the stored energy contributes to ion acceleration, affecting the overall efficiency of the thruster.

Refinements have been proposed by researchers like Burton [40] to derive more accurate thrust values. For coaxial PPTs, the thrust contributions are calculated as.

1. Electrothermal Thrust (I_{ET})

$$I_{ET} = (\gamma - 1)\left(\frac{\Psi R}{a}\right) \tag{26}$$

2. Electromagnetic Thrust (I_{EM})

$$I_{EM} = \Psi\left(\frac{\mu_0}{4\pi}\right)\left[ln\left(\frac{r_a}{r_c}\right) + C\right] \tag{27}$$

where.

- $\Psi = \int I^2 dt$ is the integral of the squared current over time ($A \cdot s$).
- C is the constant ranging from 0 to 0.75.

2. Experimental apparatus

2.1. Hanging pendulum thrust stand design

To accurately measure impulse bits in the range of 150–550 μN s, this study develops a hanging pendulum-type thrust stand designed to measure impulse bits around 350 μN s. Choosing a hanging pendulum design eliminates errors associated with metal fatigue and temperature-induced variations in spring coefficients. Additionally, the design minimizes rotational inertia, improving the precision of angular displacement measurements.

The distance L_{cm} between the center of gravity and the pivot point and the lever arm's total mass m primarily determines the thrust stand's effective spring constant k. The lever arm is fabricated from SAE 304 stainless steel to minimize the impulse energy is absorbed due to material deformation. The lever arm segment connected to the PPT was designed to reduce the distance L_t between the pivot and the thruster's thrust application point, achieving 77 mm. At the opposite end, the measurement point was placed 200 mm away from the pivot, leveraging the lever principle to maximize displacement detection.

With a height constraint of 500 mm in the vacuum chamber, careful considerations were made to ensure proper clearance and balance. A 127 mm gap was maintained between the pivot and the bottom of the thruster, while the design included an additional 100 mm safety margin to prevent interference. The remaining 253 mm was designated for counterweight positioning, allowing for precise load distribution. Adjustments to the counterweight copper plate ensured the center of gravity aligned with the pivot as closely as possible. After several refinements, the final center of gravity was positioned 18.72 mm below the pivot. The total mass of the lever arm was determined to be 0.89 kg, with a calculated rotational inertia of 0.0081 kg m^2.

$$k = k_s + mgL_{cm} = 0 + 0.89 \cdot 9.81 \cdot 0.01872 = 0.16 \tag{28}$$

A copper plate attached to the lever arm is a counterweight and an eddy current damper. This damper is positioned between two NdFeB magnets, introducing controlled damping forces. Assuming a damping ratio $\xi = 0.5$ (recommended [1] damping ratio $0.5 \le \xi \le 0.6$), the required damping coefficient c is calculated as:

$$\xi = 0.5 = \frac{c}{2}\sqrt{\frac{1}{Ik}} \Rightarrow c = 0.036 \tag{29}$$

Using a copper plate of 2 mm thickness δ and an area S of 216 mm^2, the required magnetic flux density B_z was determined as [43]:

$$c = 0.036 = F_c L_d \Big/ \left({}^{v_c}\!/_{L_d} \right) = \sigma_c \delta {B_z}^2 S \alpha_1 L_d^2 \Rightarrow B_z = 0.036 \tag{30}$$

where.

- F_c is the drag force induced by eddy current (N).
- L_d is the distance between the copper plate center and pivot (m).
- v_c is the velocity of the copper plate (${}^{m}\!/_{s}$).
- σ_c is the conductivity of the copper (${}^{S}\!/_{m}$).
- α_1 is the constant decided by copper plate geometric.

$$\alpha_1 = 1 - \frac{1}{2\pi}\left[4\tan^{-1}\left(\frac{b}{a}\right) + \frac{b}{a}\ln\left(1 + \frac{a^2}{b^2}\right) - \frac{a}{b}\ln\left(1 + \frac{b^2}{a^2}\right) \right] \tag{31}$$

where a is the length of the copper plate and b is the height of the copper plate.

NdFeB magnets with a surface magnetic flux of 0.014 T were chosen to meet the system's requirements. Since the distance between the magnets and the copper plate can be freely adjusted, the desired magnetic flux can be controlled by modifying this spacing.

By substituting the effective damping coefficient c, spring constant k, and lever arm inertia I into the motion equations, the expected system behavior was modeled (Fig. 6).

Since the measurement point was positioned 200 mm from the pivot, the resulting displacement range was between 34 μm and 126 μm. Given these values, this study selected a Panasonic HL-G103-A-C5 laser displacement sensor (resolution 0.5 μm) for measurement. To minimize electromagnetic interference (EMI) from PPT discharges, a custom sensor mounting base was designed using SAE 304 stainless steel. The sensor is secured using M3 screws, while an M-shaped connector enables attachment via M4 screws. This setup provides a robust and reliable platform for evaluating impulse bit of PPT in a vacuum environment.

2.2. Electrostatic comb design and calibration

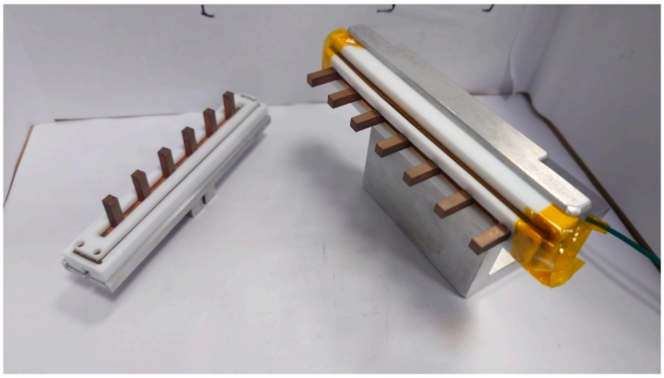

Fig. 7. The electrostatic comb, the left one mounted on the lever arm and the right one fixed to the thrust stand frame.

The electrostatic comb (ESC) is used to generate standardized thrust impulses for calibration. Fig. 7 illustrates the ESC design, which consists of two interleaved metal comb structures. One comb is mounted on the lever arm, and the other is fixed to the thrust stand frame. An electrostatic force is generated when a voltage is applied between the combs, maintaining an approximately constant separation distance. The overlapping distance is designed to be around 10 mm, and since the lever arm's oscillation amplitude is limited to ±126 μm, the variations in separation distance are negligible (see Fig. 8).

According to Eq. (17), increasing the number of comb teeth N enhances the generated electrostatic force F_{ESC} for a given input voltage. The ESC teeth are rectangular prisms with dimensions of 4 mm × 4 mm × 15 mm. These dimensions ensure structural stability and prevent deformation during manufacturing, mainly because the combs are fabricated from soft copper (C1814). The spacing between adjacent teeth within the same comb is 12 mm, allowing the interleaved structure to accommodate the opposing comb's teeth. The white ceramic (Al_2O_3) is used as an insulator, offering excellent thermal and electrical insulation to prevent electrical breakdown or discharge between the comb electrodes.

The electrostatic force produced by the ESC is proportional to the square of the input voltage. This study used an electronic balance to measure the force generated by the ESC under different voltage levels. The calibration experiment involved suspending one end of the ESC above a precision electronic balance using a 4040 aluminum extrusion while the other end was placed directly on balance. When a voltage was applied to the ESC terminals, the electrostatic attraction reduced the effective weight measured by the balance. The difference in weight was then used to determine the generated thrust. A high-precision balance was required because the target thrust measurements were in the micro-Newton range. This study selected the AP324X electronic balance due to

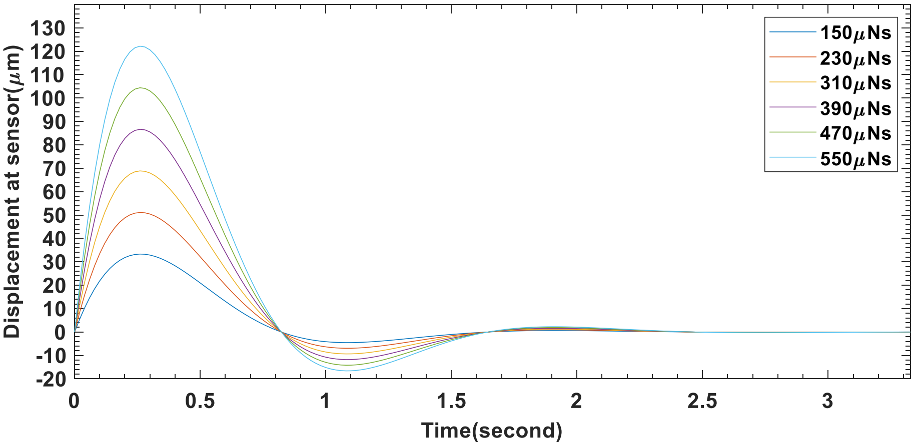

Fig. 6. Expected angle deflection variate with time for different input impulses.

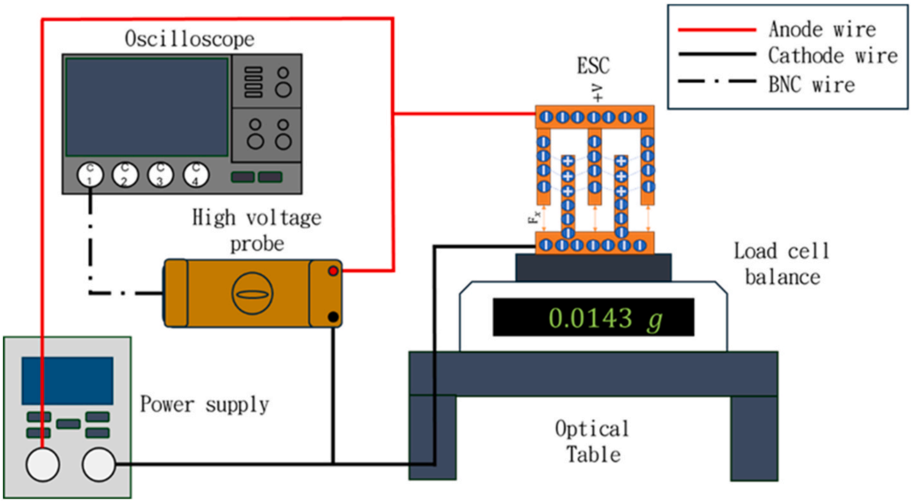

Fig. 8. Experimental setup of electrostatic comb calibration process.

its resolution of 0.1 mg, corresponding to approximately 1 μN resolution, and its error margin of ±0.3 mg. With a maximum load capacity of 320 g, the balance was more than sufficient to support the 142 g ESC. Additionally, the balance featured an internal auto-calibration function to maintain accuracy despite environmental variations such as uneven surfaces. Due to the extreme sensitivity required for micro-Newton-level force measurements, even minor environmental vibrations could introduce uncertainties. This study placed the ESC calibration setup on an Integrity 2 VCS vibration-isolated optical table to mitigate the noise. This system provides compliance values ranging from 10^{-4} to $10^{-7}\ {}^{mm}\!/_{N}$ above 100 Hz, ensuring that vibrations do not interfere with force measurements.

This study used a YS0530 high-voltage power supply to apply voltage across the ESC. Initial theoretical estimates suggested that applying 700 V would generate a thrust of approximately 100 μN, while 1300 V would produce around 400 μN. However, the actual voltage required to achieve the expected thrust values was higher than anticipated due to leakage currents and system inefficiencies. The experimental results indicated that 800 V was necessary to generate a measured force of 74 μN, while 2400 V was required to produce 418 μN. A high-voltage differential probe (DP-15K) was connected to the ESC terminals to investigate further the discrepancy between the expected and actual voltage outputs. The measurements revealed that the actual voltage was consistently lower than the set voltage, with the deviation increasing at higher voltage levels. At 800 V, the actual applied voltage was 60 V lower than the set value, while at 2400 V, the discrepancy had increased to 410 V.

Ten data points were collected between 800 V and 2400 V, increasing in 160 V increments to establish an accurate calibration curve. After applying the voltage, the balance reading was recorded once it stabilized, with no fluctuations within 1 min. The ESC was removed and reinstalled before each measurement to account for potential inconsistencies introduced by assembly variations. This process was repeated five times for each voltage level to ensure reliability. Since the electrostatic force generated by the ESC is proportional to the square of the input voltage, the balance readings were converted into corresponding standard forces and analyzed through regression against the square of the input voltage. The final regression model determined the precise conversion parameters linking the applied voltage to the generated force.

ESC in the thrust stand setup is positioned 100 mm above the pivot, while t PPT exit's center is located 77 mm below the pivot. By neglecting material deformation, the ratio of the electrostatic attraction force at the ESC to the equivalent thrust at the PPT exit is calculated to be 1.2987. For example, a weight change of 0.0074 g, corresponding to an electrostatic force of 72.59 μN, translates to an equivalent thrust of 94.27 μN at the PPT exit.

Fig. 9 (a) presents the calibration results, where the y-axis represents the equivalent thrust derived from balance readings, converted using this ratio. According to Eq. (17), the square of the applied voltage across the ESC is expected to be proportional to the electrostatic force. Since the equivalent thrust is also proportional to the electrostatic force, the equivalent thrust should exhibit a linear relationship with the square of the applied voltage. The data points align well with a straight-line trend, confirming this expected relationship. However, the regression line exhibits a negative offset at zero voltage instead of passing through the origin. The equivalent thrust shows an offset of 2.36 μN. Given that the measurement error of the electronic balance is ±0.3 mg, this offset corresponds to 0.19 mg on the balance, suggesting that this zero-point deviation is likely due to instrument error.

The conversion parameter that relates the square of the applied voltage to the equivalent thrust was determined to be $1.33 \times 10^{-10}\, {}^{N}\!/_{V^2}$. This value also corresponds to the slope of the regression line. Fig. 9 (b) presents the standardized residuals of the calibration data. The y-axis represents the residuals, the difference between the actual measured equivalent thrust and the predicted value from the regression line, normalized by the standard deviation. The x-axis represents the applied voltage levels. Most residual data points fall within the ±2 range, indicating that the residuals follow a normal distribution. This distribution confirms the statistical validity of the regression model. Based on this analysis, for a given input voltage, there is a 95 % probability that the actual output thrust will be within ±10.92 μN of the predicted thrust.

2.3. *Zaplab's pulsed plasma thruster*

As shown in Fig. 10(b), the coaxial pulsed plasma thruster targeted for measurement in this study is designed with the outer metal shell serving as both the cathode for the ignition electrode and the central discharge cathode. During the measurement process, a layer of Kapton polyimide insulation is inserted between the two to prevent electrical conductivity between the cathode and the pendulum. After being charged by the capacitor, the cathode is connected to the outer shell, while the anode is connected to the central cylindrical conductor. This setup generates a strong electric field between the outer shell and the central cylinder due to the voltage difference between the two electrodes.

Additionally, a shell layer acts as the ignition anode, which is separated from the outer shell by an insulating layer. When a high voltage is

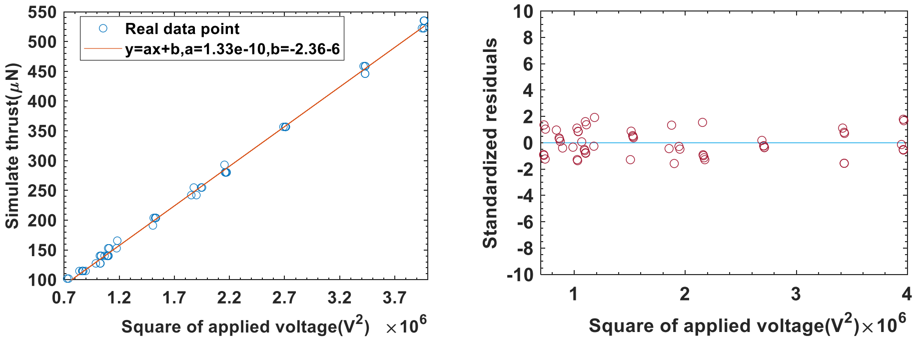

(a) (b)

Fig. 9. ESC applied voltage and simulating thrust calibration result (a) Regression line and real data of calibration result (b) Standardized residuals.

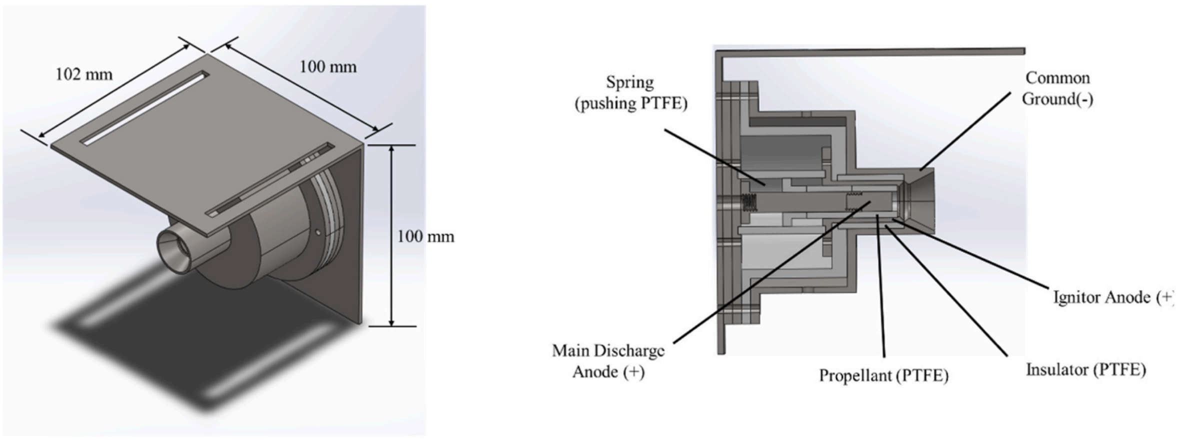

(a) (b)

Fig. 10. Diagram of Zaplab's pulsed plasma thruster (a) Scales of pulsed plasma thruster (b) Schematic of PPT's component.

applied between the ignition anode and the outer shell cathode, an electric arc is triggered, causing positive ions and electrons to form an electrical bridge in the strong electric field between the outer shell and the central cylinder. This process results in fuel ablation, generating more positive ions. These ions are then accelerated from the central cylinder towards the outer shell due to the electric field. As these ions accelerate, they generate a magnetic field. The Lorentz force acting on the positive ions due to this magnetic field then accelerates the ions, expelling them from the thruster, thereby producing thrust.

2.4. *Experimental set up*

To achieve accurate impulse measurements of PPT, it is essential to establish a precise relationship between the input impulse and the resulting angular displacement of the thrust stand.

All experiments were conducted inside a vacuum chamber to ensure the calibration process accurately replicates actual measurement conditions, evacuated to an experimental pressure of 4×10^{-5} Torr before initiating the calibration procedure.

The vacuum chamber, illustrated in Fig. 11, has an internal diameter of 1 m and a depth of 1.5 m. It is designed to simulate a near-space vacuum environment, enabling precise propulsion experiments and impulse measurements. A two-stage evacuation process is employed to achieve and maintain high-vacuum conditions 4×10^{-5} Torr. Initially, a rough pump (LS120A) reduces the pressure to 2×10^{-2} Torr. A turbomolecular pump (TGkine1700M – B) further evacuates the chamber to the target experimental pressure.

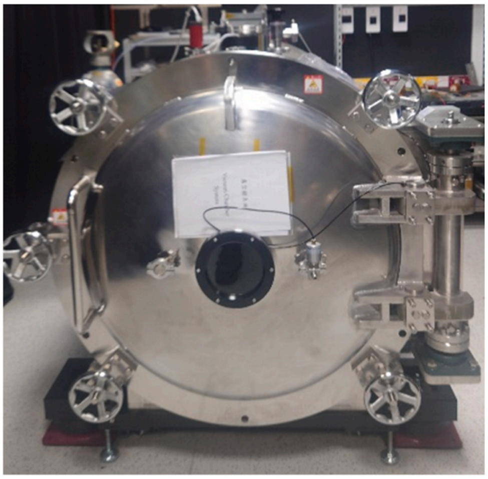

Fig. 11. Diagram of vacuum chamber for simulating high vacuum space environment.

2.4.1. *Experimental setup for hanging pendulum thrust stand calibration*

To precisely control and monitor the applied impulses, the calibration setup integrated several key components, including an oscilloscope, a high-voltage differential probe (DP-15K), and a high-voltage power supply (YS0530) for applying and recording the ESC bias voltage. Additionally, the system incorporated NI CompactRIO, which enabled precise control of the high-voltage power supply with an RS232 interface and applied pulsed bias voltages to the ESC. This system also recorded signals the laser displacement sensor returned, with a virtual instrument (VI) interface facilitating real-time calibration execution. This study chose the NI CompactRIO system over a traditional oscilloscope for signal acquisition to prevent ground loop contamination, which could introduce measurement uncertainties. Oscilloscopes use the ground level as a reference, and external electromagnetic interference from other experimental equipment could introduce signal shifts or noise. An independent battery powered the laser displacement sensor, and the NI 9205 module was employed to ensure ground isolation, allowing the sensor's output voltage to serve as a stable zero-point reference.

The wiring configuration between the PPT, circuit components, ESC, and power supply was carefully designed to minimize measurement errors (see in Fig. 12). The PPT circuit can produce discharge currents as high as 1000 A, resulting in significant electromagnetic interactions between wires. Additionally, bending points along a wire can induce Lorentz forces, potentially creating unwanted forces that affect measurements. From an engineering perspective, a standard method to mitigate electromagnetic interference (EMI) involves using coaxial cables or conductive shielding layers. However, these methods introduce mechanical challenges, such as parasitic spring and damping coefficients, which could interfere with the thrust stand's oscillation. This study opted for AWG49 wires with PTFE insulation (1.1 mm diameter) to minimize mechanical interference. Furthermore, all cables were routed close to the system's rotational axis and secured to the sides of the thrust stand. This ensured that any Lorentz forces generated would not interfere with measurement results.

The YS0530 high-voltage power supply was programmed to increase the voltage from 800 V to 2400 V in increments of 160 V. At each voltage step, the NI 9870 module controlled the YS0530 to generate a 1-s voltage pulse, which was applied to the ESC, inducing oscillation in the thrust stand's arm. The NI CompactRIO system continuously recorded position data from the laser displacement sensor. This study configured the system to automatically pause recording when the displacement voltage reached a predefined trigger threshold of 1 mV above the zero-point voltage. This feature streamlined data collection and captured significant oscillation waveforms.

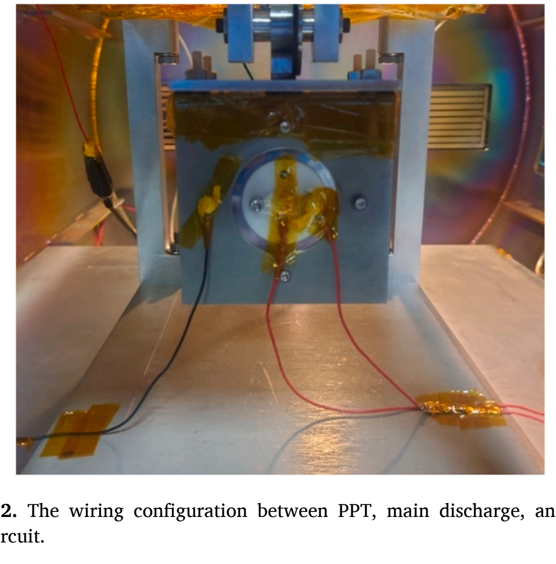

Fig. 12. The wiring configuration between PPT, main discharge, and ignition circuit.

Fig. 13 illustrates the experimental setup of the hanging pemdulum thrust stand and calibration process. The calibration process was repeated ten times for each voltage step before moving to the next voltage level. After calibration, the experiment recorded the maximum oscillation amplitude and the corresponding input pulse voltage. The input pulse voltage was converted into its corresponding total impulse by utilizing the conversion parameters obtained during the ESC calibration, which relate the square of the input voltage to the generated electrostatic force. A regression analysis was then performed between the total impulse and the maximum oscillation amplitude, yielding a precise conversion parameter that establishes the relationship between input impulse and angular displacement.

2.4.2. *Experimental setup for parameters determination*

The accuracy of thrust measurements using the thrust stand can be affected by various factors, including propellant consumption and the system's electrical connections. These factors may alter the system's physical properties, such as its spring constant, damping coefficient, and moment of inertia. Therefore, before conducting thrust measurements, verifying and quantifying these parameters is necessary to ensure their acceptability.

In an ideal spring-damper system, the oscillation waveform of the thrust stand is primarily influenced by three key parameters.

- Effective spring constant: It determines the restoring force acting on the system.
- Effective damping coefficient: It governs the energy dissipation of oscillations.
- Moment of inertia: It affects the rotational dynamics of the system.

The spring constant can be determined by applying a series of fixed thrusts and recording the corresponding angular displacements. The moment of inertia is derived from the acceleration resulting from these displacements. The effective damping coefficient, however, cannot be measured directly; instead, it is extracted indirectly by analyzing the damped oscillation frequency ω_d of the system (see Fig. 14).

Fig. 15 presents the experimental setup used to determine the spring constant k and moment of inertia I. Since determining k requires only fixed thrusts, there was no need to use the NI CompactRIO system for pulse generation. This experiment was conducted inside a vacuum chamber to ensure consistency with actual measurement conditions, evacuated to experimental pressure.

The YS0530 high-voltage power supply was programmed to increase from 800 V to 2400 V in increments of 160 V. At each voltage step, a fixed voltage was applied, and the NI CompactRIO recorded the resulting movement of the thrust stand's force arm. The experiment repeated each voltage step five times to prove measurement reliability. This study conducted regression analysis between the angular displacement and the electrostatic force, which allowed for the determination of the ratio of torque to angular displacement, yielding the effective spring constant. Additionally, experimental data provided information about the time required for the angular displacement to reach stabilization under different electrostatic forces. The acceleration values were extracted from the rising waveforms by applying the basic acceleration formula. A regression analysis between the acceleration values and the corresponding electrostatic force provided the ratio required to determine the moment of inertia.

With both the moment of inertia I and spring constant k known, the oscillation behavior of the force arm was analyzed for each experimental condition. The recorded oscillations were subjected to Fourier transform analysis, allowing the damped oscillation frequency ω_d to be extracted. The effective damping coefficient c was calculated with the measured oscillation frequency and the system's design parameters. Fig. 15 provides a schematic representation of the experimental setup used for parameter determination.

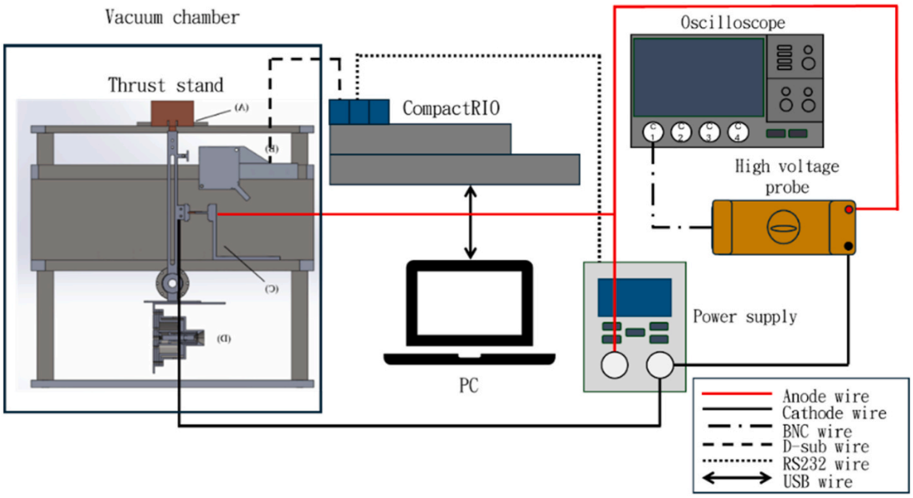

Fig. 13. Experimental setup of the hanging pendulum thrust stand calibration process.

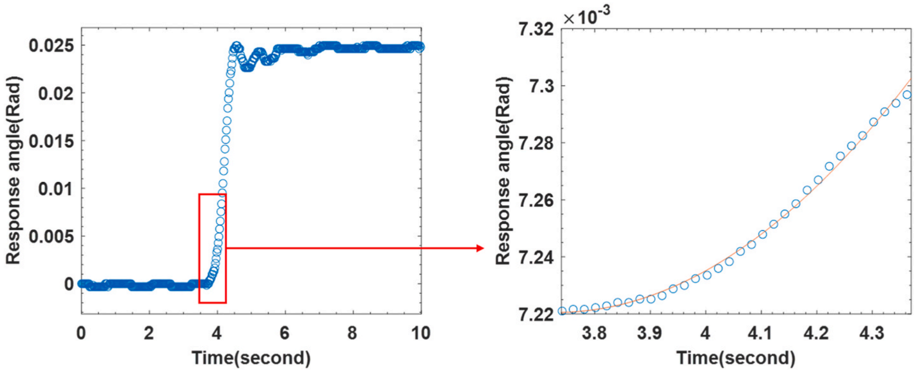

Fig. 14. Schematic of angular acceleration determined by curve fitting.

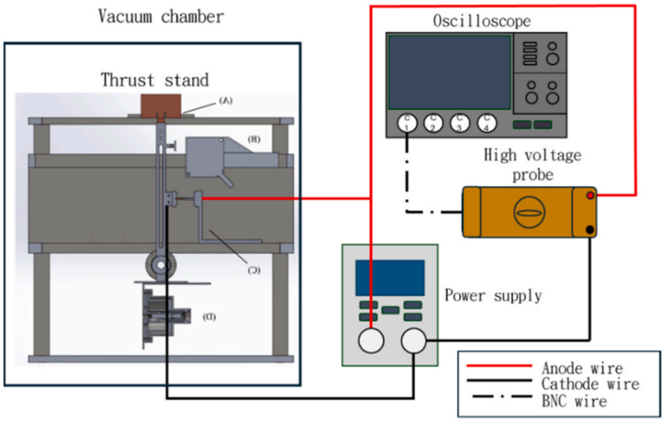

Fig. 15. Experimental setup of hanging pendulum thrust stand parameters determination.

2.4.3. *Experimental setup for impulse bit measurement*

A precise experimental setup is required to measure the impulse generated by PPT accurately. This section describes the PPT ignition and primary discharge circuits and the measurement methodology for determining impulse bits using the calibrated thrust stand.

The PPT ignition circuit and primary discharge circuit are illustrated in Fig. 16. The ignition circuit generates an arc discharge between its anode and cathode, which are connected to the PPT's outer shell and second stainless steel layer, respectively. This arc discharge, occurring at a breakdown voltage of approximately 600–800 V, heats the PTFE fuel, converting it into fuel vapor. Once the thruster chamber is sufficiently filled with vaporized fuel, the primary discharge circuit generates a high-voltage arc between the cathode (connected to the outer shell) and anode (connected to the central rod), accelerating the ionized fuel vapor to produce thrust.

The ignition circuit is based on a boost circuit consisting of diodes and inductors. With an input voltage of 30 V, supplied by a DPS3010 power supply (220 W max output), the inductor stores 0.2 J of energy. When a BNC Model 565 Pulse/Delay Generator outputs a trigger pulse, the IGBT switch in the ignition circuit releases the stored energy, generating an instantaneous 2 kV voltage pulse across the igniter terminals. Given that the breakdown voltage of the igniter is only 600–800 V, this high-voltage pulse immediately initiates an arc discharge.

The primary discharge circuit comprises a parallel capacitor and a high-voltage boost circuit. The input voltage of 30 V, supplied by a TP3020 power supply (600 W max output), is boosted to 2 kV and applied to the parallel capacitor. When the fuel vapor is ionized and the breakdown voltage between the cathode and anode falls below 2 kV, the capacitor discharges, accelerating the ionized fuel vapor and generating thrust.

The experimental setup, shown in Fig. 17, incorporates a voltage and current measurement system to analyze the discharge characteristics of the PPT. The circuit connected to the positive terminal of the main electrodes passes through a 301X current monitor, which records the temporal variation of the discharge current from the capacitor. Additionally, a high-voltage differential probe (DP-15K) measures the

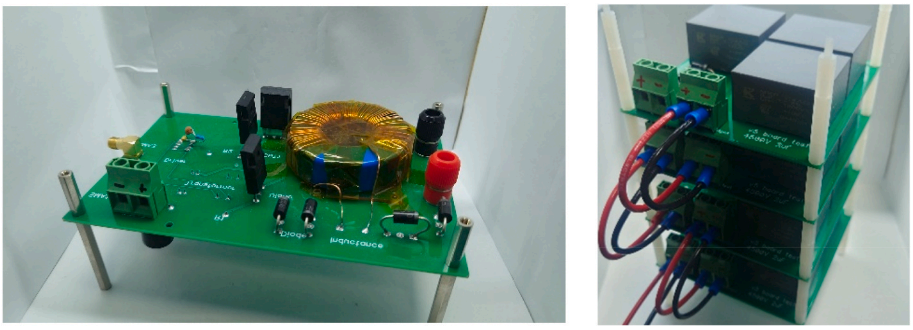

(a)

(b)

Fig. 16. Power processing unit of pulsed plasma thruster (a) ignition circuit (b) main discharge circuit.

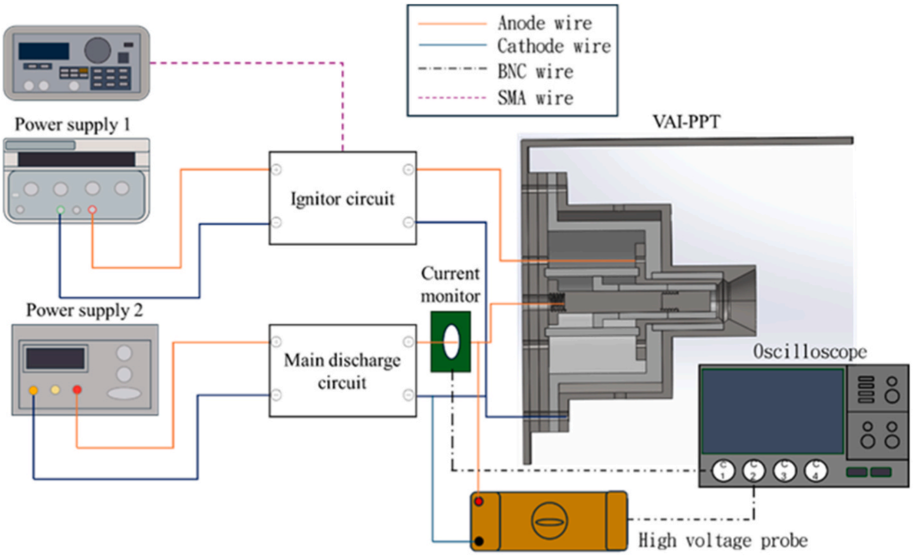

Fig. 17. Experimental setup of PPT power processing and discharge parameters recording.

potential difference between the main electrodes over time. This measurement system provides a high-resolution, time-dependent analysis of the PPT discharge process, ensuring that the electrical characteristics of each impulse are precisely recorded.

Following the thrust stand calibration, the article established the conversion parameters between input impulse and maximum angular displacement. The PPT impulse per shot was measured and validated with the conversion parameters. The experimental setup for PPT performance measurement is streamlined only to include the NI CompactRIO system, which manages to trigger the discharge event and record angular displacement data. During the experiment, the main discharge energy of the PPT varied from 12 J to 28 J in 4 J increments. The resulting angular displacement of the thrust stand was recorded for each energy level, and the total impulse per shot was calculated using the pre-established calibration parameters.

3. Testing and result

3.1. *Calibration result of hanging pendulum thrust stand*

Since the laser displacement sensor's output voltage is proportional to its measurement position, any impulse applied to the thrust stand's lever arm will induce oscillations, which are recorded as voltage fluctuations over time. These oscillations represent the angular displacement of the lever arm. Fig. 19 (a) illustrates this relationship, where the y-axis represents the peak voltage deviation from the zero point. At the same time, the x-axis corresponds to the standard impulse generated by the ESC. Although the data points are not uniformly distributed, they align with the expected linear regression model, as Eq. (10) predicted (see Fig. 1).

During calibration, this study programmed NI CompactRIO controlling ESC to apply a 320 μN s impulse with a pulse width of 1 s, as shown in Fig. 20 (a). The impulse force profile over time was derived from high-voltage probe measurements of the ESC terminal voltage. However, repeated trial analysis revealed that the pulse width varied between 0.7 and 1.1 s, introducing inconsistencies in the impulse application.

This variability is attributed to the control method used for generating voltage pulses. The NI CompactRIO system controls the YS0530 high-voltage power supply using a straightforward ON/OFF switching mechanism. When the CompactRIO triggers the YS0530 output, a timer starts counting, and after 1 s, another signal is sent to terminate the voltage output. Given that NI CompactRIO features a 20 MHz timer with a resolution of 50 ns, its timing accuracy is not in question. The RS232 communication protocol, operating at 19200 bps, also follows manufacturer specifications.

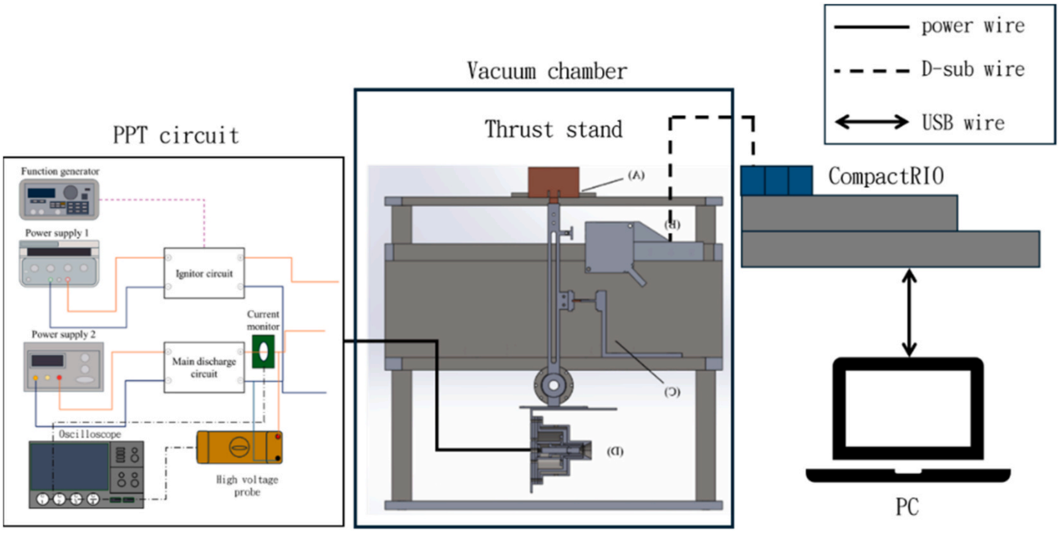

Fig. 18. Experimental setup of PPT impulse bit measurement.

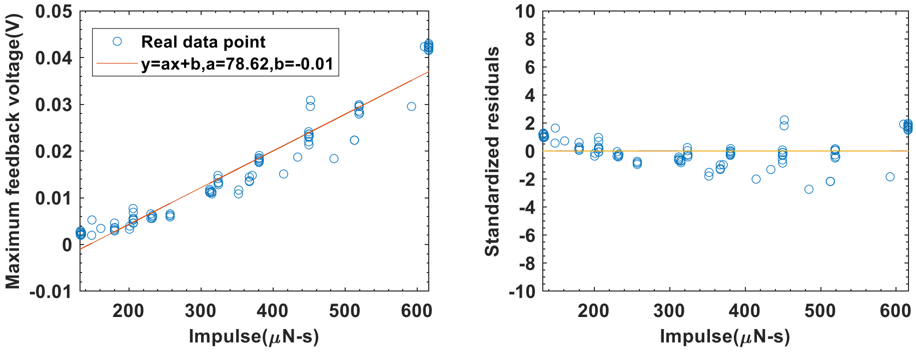

(a)

(b)

Fig. 19. Thrust stand maximum angular displacement and input standard total impulse calibration result (a) Regression line and real data of calibration result (b) Standardized residuals.

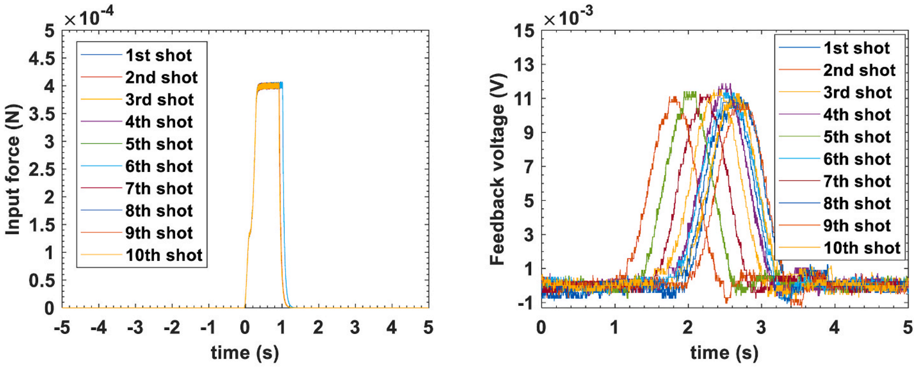

(a)

(b)

Fig. 20. Standard impulse of ESC (expected impulse 320 μN s) and response voltage signal from thrust stand variation over time (a) The electrostatic force over time (b) The response voltage signal of thrust stand over time after input impulse.

The most probable cause of the pulse width variation is the response time of the YS0530 power supply. When generating high voltages, its internal components require a finite amount of time to charge up to the target voltage. Similarly, when voltage output is terminated, there is a delay in circuit cutoff, leading to slight variations in actual pulse duration. As a result, even though the YS0530 receives the trigger signal immediately, it takes time to reach the desired voltage, and similarly, there is a lag before it completely stops outputting. This discrepancy explains the non-uniform distribution of data points in Fig. 19 (a).

Fig. 20 (b) displays the voltage response relative to the zero-point voltage from the laser displacement sensor. Since the NI CompactRIO system records data based on voltage triggers, each dataset has a slightly different initial time reference, leading to time shifts among oscillation waveforms. However, this does not impact calibration results because only the peak values of oscillations are used for analysis.

Electrical noise in the system introduces ripple fluctuations, which affect the calculation of peak values. The fluctuations sometimes increase the apparent maximum displacement, artificially inflating the calculated peak values. In the other cases, the fluctuations decrease the apparent maximum displacement, leading to lower calculated peak values. Additionally, variability in the applied impulse (ranging between 221 and 282 μN s) causes slight differences in peak values across trials. The abovementioned conditions explains why some data points in Fig. 18 deviate slightly above or below the regression line.

A more significant deviation is observed in the data points for 132 μN s and 615 μN s in Fig. 19 (a), which cluster in the upper-left region of the regression line rather than aligning with predicted values. Fig. 21 provides insight into this behavior by showing these impulse levels' time-dependent sensor voltage response.

In Fig. 21 (b) (615 μN s input), the force arm displacement is relatively large, resulting in clear oscillations dominating noise fluctuations. Consequently, the sensor's voltage response is smooth, with negligible ripple effects. Conversely, Fig. 21 (a) (132 μN s input) exhibits small displacements (~1.81 μm), making it difficult for the HL-G103-A-C5 laser displacement sensor to capture the oscillatory motion fully. This results in fragmented voltage readings rather than a continuous oscillation waveform. Although smaller displacements lead to missing data points, they do not significantly impact peak values. Across 10 experimental trials of 132 μN s input, all peak values exceeded 0.5 μm, demonstrating consistent detection. Additionally, more significant input impulses produce higher voltage displacements, making ripple effects less significant. This result confirms that the clustering of data points in the upper-left region of the regression line is not a measurement error but a consequence of other unknown factors.

3.2. *Determination of thrust stand parameters*

The regression model assumes in Eq. (10) is that key physical parameters, including the damping coefficient *c*, spring constant *k*, and moment of inertia *I*, remain constant throughout the calibration process. However, specific data points at 132 μN s and 615 μN s deviated from the expected trend. This section investigates the physical parameters of the thrust stand when installed in the vacuum chamber, aiming to explain these deviations. After the initial calibration, the experiment modified the experimental setup to apply constant force using ESC rather than pulsed thrust. The thrust stand parameters were then determined by analyzing the angular acceleration at the moment of force application and the final angular displacement achieved when the applied force balanced the gravitational torque.

Fig. 22 (a) presents the relationship between applied torque and angular acceleration. The y-axis represents the ESC-producing torque, which is computed based on the voltage applied across its terminals. Since the ESC is rigidly attached to the pendulum arm, its generated force directly contributes to the system's torque. The x-axis represents the angular acceleration derived from fitting the laser displacement sensor's feedback data to a second-order kinematic equation. Although individual data points exhibit some scatter due to random measurement variations, they remain centered around the regression line, with a correlation coefficient of 0.6966, indicating a strong positive correlation between applied torque and angular acceleration. According to the definition of the moment of inertia *I*, which is the ratio of applied torque to the resulting angular acceleration, the results confirm that within the torque range of 15.8 μN m to 70.9 μN m, the moment of inertia remains unchanged. These two torque ranges correspond to the impulse range of 132 μN s to 615 μN s, the same range where deviations were observed during calibration.

Fig. 22 (b) presents the relationship between applied torque and angular displacement after the oscillations have settled. The y-axis represents the applied torque, while the x-axis represents the steady-state angular displacement relative to the zero position. According to the definition of effective spring constant *k*, which is the ratio of applied torque to angular displacement, the regression slope in Fig. 22 (b) directly represents the thrust stand's effective spring constant. Unlike Fig. 22 (a), where data points show more scatter, the x-axis values in Fig. 22 (b) are taken after oscillations settle, reducing randomness and yielding a higher correlation coefficient of 0.9704. However, Fig. 22 (b) shows that data points at 15.8 μN m and 70.9 μN m deviate downward from the regression line. At 15.8 μN m, the torque is too small to induce noticeable deformation in the cables connecting the PPT to the thrust stand. The cable's effect leads to a smaller-than-expected increase in angular displacement. At 70.9 μN m, the applied torque exceeds the linear operating range, causing larger-than-expected angular displacements. This observation explains why, during thrust stand calibration, the impulse responses at 132 μN s and 615 μN s exhibited departure from the regression line.

To further investigate this phenomenon, Fast Fourier Transform (FFT) analysis was performed on the impulse response waveforms at 132 μN s, 320 μN s, and 615 μN s, as shown in Fig. 23.

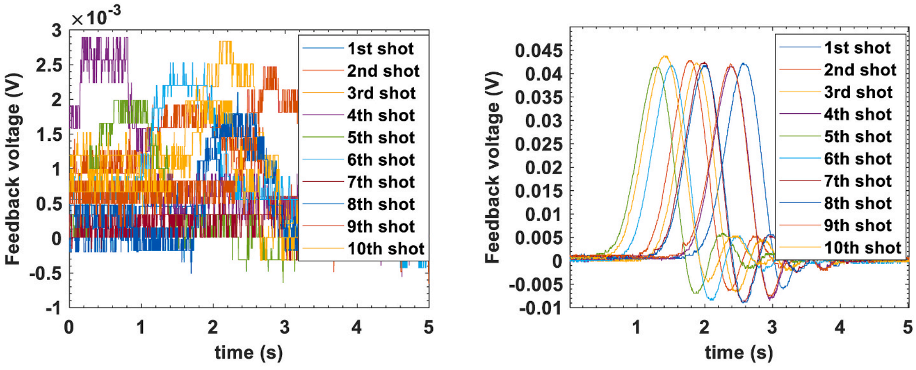

(a) (b)

Fig. 21. Response voltage signal from thrust stand variation over time (a) Input impulse 132 μN s (b) Input impulse 615 μN s.

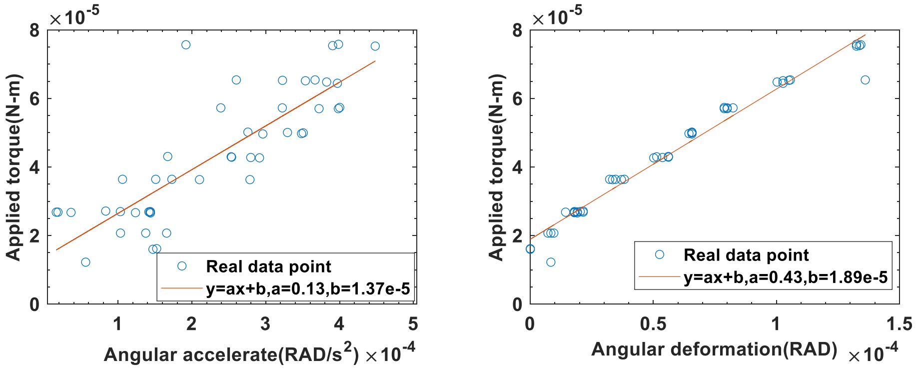

(a) (b)

Fig. 22. Determination results of spring constant and pendulum inertia (a) Applied torque and relative angular acceleration (b) Applied torque and relative angular deformation.

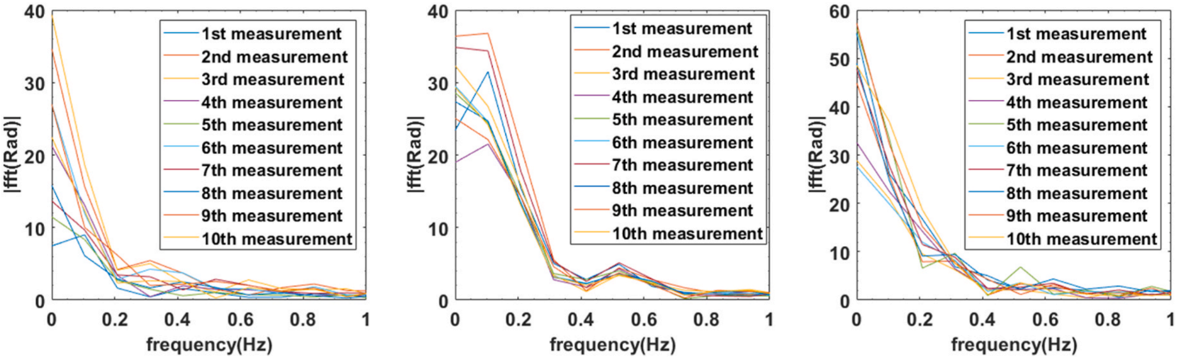

(a) (b) (c)

Fig. 23. Fast Fourier transform of response voltage signal from thrust stand over time after input impulse (a) 132 μN s (b) 320 μN s (c) 615 μN s.

Fig. 23 (b) presents the FFT result for the 320 μN s impulse response, which falls within the linear region of the system. The peak observed in the 0.4–0.7 Hz range corresponds to the fundamental oscillation frequency of the thrust stand following impulse application. The dominant peak at 0.52 Hz is consistent with the oscillation period observed in time-domain data (approximately 1.9 s per cycle in Fig. 20 (b)). Additional frequency components above 0.7 Hz are attributed to electrical noise and do not significantly contribute to the mechanical response.

Unlike the 320 μN s case, the FFT results for 132 μN s (Fig. 23 (a)) and 615 μN s (Fig. 23 (c)) reveal inconsistent frequency responses. In Fig. 23 (a), only the 7th and 9th experimental trials exhibit a dominant peak at 0.52 Hz, while other trials show peaks in the 0.3–0.4 Hz range. Given that the natural frequency ω_n is determined by the spring constant k and moment of inertia I, reducing the effective spring constant would lower the damped oscillation frequency ω_d, as described in Eq (8). This scenario matches the observed shift in dominant frequencies. A similar trend is seen in Fig. 23 (c), where only the 5th trial retained a dominant peak at 0.52 Hz, while others shifted to 0.31 Hz. The frequency shifting confirms that variations in the effective spring constant influenced the impulse response at 132 μN s and 615 μN s, causing the calibration data points for these impulses to deviate from the regression line.

To further quantify these deviations, Table 1 compares the ideal design parameters of the thrust stand with the experimentally measured parameters within the impulse range of 180–518 μN s, where the system maintains linear behavior (see Table 2).

Although the measured damping ratio does not fall within the 0.5–0.7 range, it remains less than 1, indicating that the system is still

Table 1
Comparison between ideal parameters of design thrust stand and real parameters of experimental thrust stand.

	Ideal parameters	Real parameters
Spring constant k	0.16 $\text{Nm}/_{\text{rad}}$	0.43 $\text{Nm}/_{\text{rad}}$
Moment of inertia I	0.008 kgm^2	0.127 kgm^2
Damped frequency ω_d	3.77 Hz	0.52 Hz
Natural frequency ω_n	4.47 Hz	1.84 Hz
Damping ratio ξ	0.5361	0.96
Damping constant c	0.036 $\text{Nms}/_{\text{rad}}$	0.448 $\text{Nms}/_{\text{rad}}$

Table 2
Error budget summary due to system parameters.

Relative uncertainty	Value
$\delta B_{stand,ran}/_{B_{stand}}$	0.1329
$\delta L_t/_{L_t}$	0.071
$\dfrac{\delta B_{stand,sys}}{\delta I}\dfrac{\delta I}{B_{stand}}$	0.0387
$\dfrac{\delta B_{stand,sys}}{\delta k}\dfrac{\delta k}{B_{stand}}$	0.023
$\dfrac{\delta B_{stand,sys}}{\delta c}\dfrac{\delta c}{B_{stand}}$	0.011
$\delta B_V/_{B_V}$	0.001
$\delta V_m/_{V_m}$	0.079

underdamped and can be modeled using underdamped system equations. However, the spring constant and damping coefficient were significantly higher than expected, affecting system dynamics.

The discrepancy in the spring constant can be attributed to the actual thrust stand mass being 1.22 kg instead of the expected 0.89 kg. This increase was due to additional components such as screws and mounting fixtures. If only gravitational torque contributed to the spring constant, its expected value would be 0.22 N m/rad, which accounts for only 51 % of the measured value. The remaining spring force contribution likely originates from the electrical cables connecting the PPT to the thrust stand. These cables introduce parasitic spring and damping effects [25], which vary depending on the applied torque. The cable parasitic effects explain why the effective spring constant was inconsistent at specific torque levels. Additionally, the high parasitic damping coefficient from the cables reduced the influence of the eddy current damper's influence, accounting for only 8 % of the total damping effect. Consequently, adjusting the magnet spacing in the eddy current damper did not significantly alter the damping behavior.

3.3. *Uncertainty analysis of impulse bits measurements*

As shown in Fig. 19 (a), within the input impulse range of 180–518 μN s, there is a linear relationship between the input impulse I_{bit} and the maximum response voltage difference V_m, expressed as

$$V_m = B_{stand} I_{bit} \tag{32}$$

From a thrust stand parameter perspective, the conversion parameter B_{stand}, which relates the input impulse to the maximum response angle, is influenced by several physical parameters: the moment of inertia I, effective spring constant k, effective damping coefficient c, distance from the thrust center to the pivot L_t, and the displacement sensor conversion parameter B_v

$$B_{stand} = e^{-\frac{\xi}{\sqrt{1-\xi^2}} tan^{-1}\left(\frac{\sqrt{1-\xi^2}}{\xi}\right)} \frac{L_t B_V}{I\omega_n} = e^{-\frac{c}{\sqrt{4Ik-c^2}} tan^{-1}\left(\frac{\sqrt{4Ik-c^2}}{c}\right)} \frac{L_t B_V}{\sqrt{Ik}} \tag{33}$$

By rearranging the equation, the input impulse I_{bit} can be derived as

$$I_{bit} = \frac{V_m}{B_{stand}} = e^{\frac{c}{\sqrt{4Ik-c^2}} tan^{-1}\left(\frac{\sqrt{4Ik-c^2}}{c}\right)} \frac{\sqrt{Ik}}{L_t B_V} V_m \tag{34}$$

Using error propagation theory [44], the fractional uncertainty in impulse measurement is given by:

$$\frac{\delta I_{bit,des}}{I_{bit}} = \sqrt{\left(\frac{\delta B_{stand,ran}}{B_{stand}}\right)^2 + \left(\frac{\delta L_t}{L_t}\right)^2 + \left(\frac{\delta I_{bit,des}}{\delta I}\frac{\delta I}{I_{bit}}\right)^2 + \left(\frac{\delta I_{bit,des}}{\delta k}\frac{\delta k}{I_{bit}}\right)^2 + \left(\frac{\delta I_{bit,des}}{\delta c}\frac{\delta c}{I_{bit}}\right)^2 + \left(\frac{\delta B_V}{B_V}\right)^2 + \left(\frac{\delta V_m}{V_m}\right)^2} \tag{35}$$

Here, $\delta B_{stand,ran}$ represents the random uncertainty of the conversion parameter B_{stand}, which arises from unpredictable factors such as measurement errors, human errors, and external noise [45]. This uncertainty can be estimated using calibration data:

$$\delta B_{stand,ran} = \frac{\sigma_y}{\sqrt{\sum (x_t - \overline{x})^2}} \tag{36}$$

where:

$$\sigma_y = \sqrt{\frac{\sum_{t=1}^{n} \left(Y_t - B_{stand} x_t - B_{stand,0}\right)^2}{n-2}} \tag{37}$$

Each component contributing to uncertainty is evaluated separately.

- **Thrust Center-to-Pivot Distance L_t:** The thrust center position varies within $\pm 5.4 \times 10^{-3}\ m$ since each PPT firing occurs at a slightly different position. This introduces an uncertainty δL_t in impulse measurement.
- **Moment of Inertia I:** The moment of inertia is only affected by fuel burn-off. Even if the entire fuel block were consumed, the maximum reduction would be $1.296 \times 10^{-5} kg{\cdot}m^2$, which is negligible. Given that the fuel consumption per PPT firing is only 50 μg (total is 2 g), the real-time change in I is much smaller than the theoretical maximum. The random uncertainty δI of the moment of inertia is estimated to be $\pm 0.0285 kg{\cdot}m^2$ from experimental data of Fig. 22 (a).

The uncertainty contribution of the moment of inertia I is described by:

$$\frac{\delta B_{stand,ran}}{\delta I}\frac{\delta I}{B_{stand}} = \left\{ B_v L_t \exp\left(-\frac{c \tan^{-1}\frac{\sqrt{4Ik-c^2}}{c}}{\sqrt{4Ik-c^2}}\right) \left[\frac{V_m \exp\left(\frac{c \tan^{-1}\frac{\sqrt{4Ik-c^2}}{c}}{\sqrt{4Ik-c^2}}\right) \sqrt{Ik} \left(\frac{2k}{\left(\frac{4Ik-c^2}{c^2}+1\right)(4Ik-c^2)} - \frac{2ck \tan^{-1}\frac{\sqrt{4Ik-c^2}}{c}}{(4Ik-c^2)^{3/2}}\right)}{B_v L_t} + \frac{V_m k \exp\left(\frac{c \tan^{-1}\frac{\sqrt{4Ik-c^2}}{c}}{\sqrt{4Ik-c^2}}\right)}{2B_v L_t \sqrt{Ik}} \right] \right\} \delta I \Big/ V_m \sqrt{Ik} \tag{38}$$

- **Effective Spring Constant k:** Like the moment of inertia, k is only affected by fuel burn-off. The maximum possible reduction in k is $1.5 \times 10^{-3} Nm/_{rad}$, which is small enough to be ignored. The random uncertainty δk is estimated as $\pm 0.0575\,{}^{Nm}/_{rad}$ from experimental data of Fig. 22 (b).

The uncertainty contribution of effective spring constant k is described by:

$$\frac{\delta B_{stand,ran}}{\delta k}\frac{\delta k}{B_{stand}}=\left\{B_v L_t \exp\left(-\frac{c\tan^{-1}\frac{\sqrt{4Ik-c^2}}{c}}{\sqrt{4Ik-c^2}}\right)\right.$$

$$\left[\frac{IV_m\exp\left(\frac{c\tan^{-1}\frac{\sqrt{4Ik-c^2}}{c}}{\sqrt{4Ik-c^2}}\right)}{2B_vL_t\sqrt{Ik}}+\frac{V_m\exp\left(\frac{c\tan^{-1}\frac{\sqrt{4Ik-c^2}}{c}}{\sqrt{4Ik-c^2}}\right)\sqrt{Ik}\left(\frac{2I}{\left(\frac{4Ik-c^2}{c^2}+1\right)(4Ik-c^2)}-\frac{2Ic\tan^{-1}\frac{\sqrt{4Ik-c^2}}{c}}{(4Ik-c^2)^{3/2}}\right)}{B_vL_t}\right]$$

$$\left.\right\}\delta k\Big/V_m\sqrt{Ik} \tag{39}$$

- **Effective Damping Coefficient c:** The damping coefficient remains constant throughout impulse measurements. However, the oscillation frequency varies slightly between 0.42 Hz and 0.62 Hz, leading to a random uncertainty δc of $\pm 0.0075\,{}^{Nm\cdot s}/_{rad}$.

The uncertainty contribution of effective spring constant c is described by:

$$\frac{\delta B_{stand,ran}}{\delta c}\frac{\delta c}{B_{stand}}=\left[\frac{\tan^{-1}\frac{\sqrt{4Ik-c^2}}{c}}{\sqrt{4Ik-c^2}}+\frac{c^2\tan^{-1}\frac{\sqrt{4Ik-c^2}}{c}}{(4Ik-c^2)^{3/2}}-\frac{c\left(\frac{\sqrt{4Ik-c^2}}{c^2}+\frac{1}{\sqrt{4Ik-c^2}}\right)}{\left(\frac{4Ik-c^2}{c^2}+1\right)\sqrt{4Ik-c^2}}\right]\delta c \tag{40}$$

- **Sensor Conversion Parameter B_v:** The laser displacement sensor (HL-G103-A-C5) has a linearity error of ±0.1 %, contributing directly to the uncertainty fraction.
- **Maximum Voltage Measurement V_m:** The NI CompactRIO voltage measurement module (NI 9205) has a resolution of 0.096 mV, with a measurement error of ±0.237 mV. Given that the minimum feedback voltage recorded during calibration was 3 mV, the maximum uncertainty fraction for V_m is 0.079.

Combining these uncertainties, the fractional uncertainty in impulse measurement due to system parameters is:

$$\frac{\delta I_{bit,des}}{I_{bit}}=0.176 \tag{41}$$

From a calibration perspective, the input impulse I_{bit} of calibration is influenced by the square of the measured voltage between combs V^2, the ESC conversion parameter B_{ESC} between the square of the measured voltage V^2 and the calibration force F_{ESC}, and pulse width t_d

$$I_{bit}=t_dF_{ESC}=t_dB_{ESC}V^2=t_d2N\varepsilon_0\left[2.2464-\frac{(l_2+l_3)}{\pi x_0}\right]V^2 \tag{42}$$

where the ESC conversion parameter B_{ESC} depends on electrostatic comb geometry, including the tooth gap $2l_2$, tooth width $2l_3$, number of teeth N, and engagement depth x_0, which only engagement depth x_0 would alter throughout the calibration.

Using error propagation [44], the fractional uncertainty due to calibration is:

$$\frac{\delta I_{bit,cal}}{I_{bit}}=\sqrt{\left(\frac{\delta B_{ESC,ran}}{B_{ESC}}\right)^2+\left(\frac{2.2464+\frac{(l_2+l_3)}{\pi {x_0}^2}}{2.2464-\frac{(l_2+l_3)}{\pi x_0}}\delta x_0\right)^2+\left(\frac{\delta t_d}{t_d}\right)^2+\left(2\frac{\delta V}{V}\right)^2} \tag{43}$$

where.

- **Random error of ESC conversion parameter:** Derived from ESC calibration data in Fig. 9 using statistical analysis

$$\delta B_{ESC,ran}=\frac{\sigma_y}{\sqrt{\sum(x_t-\overline{x})^2}} \tag{44}$$

which:

$$\sigma_y=\sqrt{\frac{\sum_{t=1}^{n}\left(Y_t-B_{ESC}x_t-B_{ESC,0}\right)^2}{n-2}} \tag{45}$$

- **Depth of Engagement x_0:** The maximum variation in x_0 is $\pm 1.6364\times 10^{-5}\ m$, which results in a negligible fractional uncertainty $\frac{2.2464+\frac{(l_2+l_3)}{\pi {x_0}^2}}{2.2464-\frac{(l_2+l_3)}{\pi x_0}}\delta x_0$ of 2.28×10^{-4}.
- **Pulse Width t_d:** The ideal pulse width is 1s, but the actual range varies from 0.96s to 1.24s, introducing an uncertainty δt_d of $\pm 0.24\ s$.
- **The Measured Voltage between Combs V:** The DP-15K high-voltage probe has a ±2 % accuracy, contributing directly to the uncertainty fraction.

Combining these factors, the fractional uncertainty due to calibration is (Table 3):

$$\frac{\delta I_{bit,cal}}{I_{bit}}=0.2409 \tag{46}$$

According to the literature [46], the total uncertainty is given by:

Table 3
Error budget summary due to calibration.

Relative uncertainty	Value
$\boldsymbol{{}^{\delta B_{ESC,ran}}/_{B_{ESC}}}$	0.0072
$\boldsymbol{{}^{\delta t_d}/_{t_d}}$	0.24
$\boldsymbol{{}^{\delta V}/_{V}}$	0.02

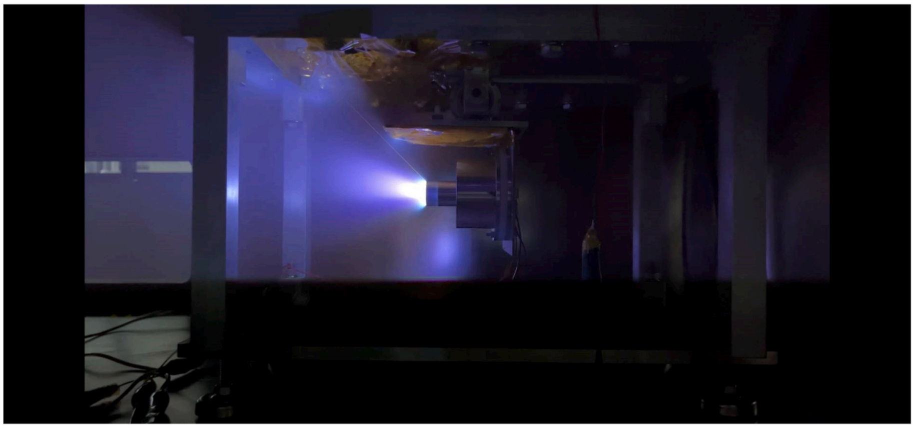

Fig. 24. Impulse measurement of PPT single firing with input energy 20J

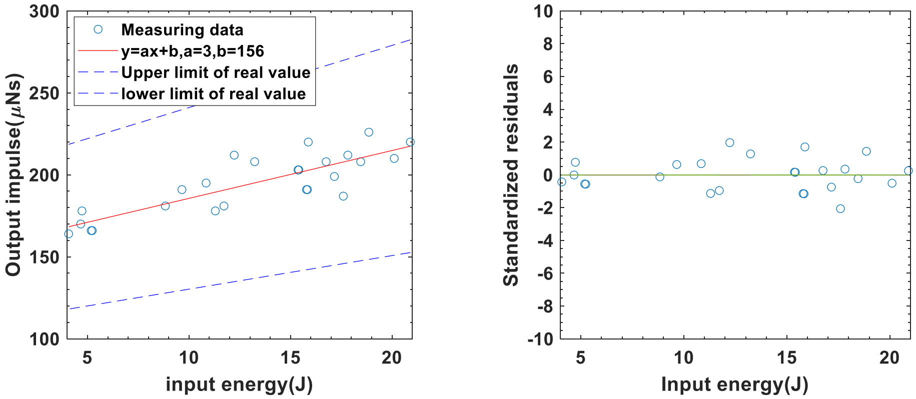

(a) (b)

Fig. 25. Measurement impulse versus the input energy of PPT (a) real data and regression line (b) standardized residuals versus input energy.

$$\frac{\delta I_{bit}}{I_{bit}} = \sqrt{\left(\frac{\delta I_{bit,des}}{I_{bit}}\right)^2 + \left(\frac{\delta I_{bit,cal}}{I_{bit}}\right)^2} = 0.2983 = 29.83\% \tag{47}$$

This analysis reveals that the most significant contributor to uncertainty (24.09 %) comes from variations in pulse width during calibration. The power supply's response time and delays in executing RS232 commands led to inconsistent pulse widths, affecting the uniformity of impulse application. Additionally, the cables introduced parasitic stiffness and damping, increasing random conversion factor uncertainty to 13.29 %.

3.4. Impulse measurement of pulsed plasma thruster

Following the impulse calibration and thrust stand parameter validation, the relationship between impulse and maximum angular displacement has been determined to be 78.62 rad/N·s. Additionally, the uncertainty in single-shot PPT impulse measurement has been quantified as ±29.83 %. The experiment was conducted in a vacuum chamber maintained at 4×10^{-5} Torr. The PPT was tested at energy levels ranging from 4 J to 20 J, with increments of 4 J. At each energy level, the PPT was fired five times, and for each firing, the input energy and corresponding angular displacement of the thrust stand were recorded. The experiment then computed the total impulse per shot from the measured angular displacement.

In Fig. 24, the y-axis represents the impulse derived from the thrust stand's angular displacement after a single PPT firing. The x-axis represents the input energy, calculated using high-voltage probes and current sensors connected across the PPT discharge electrodes. Many data points near 4 J input energy exceed 4 J in actual measured values. This discrepancy arises because the power supply that charges the capacitor was not electrically isolated from the capacitor during discharge. Consequently, additional energy was supplied during the discharge event, leading to higher input energy than the pre-set capacitor discharge value (see Fig. 25).

Additionally, each PPT firing erodes fuel at a slightly different location and amount, causing thrust direction and magnitude variability. Since the thrust stand only measures thrust along the axial direction of the PPT, any thrust components not aligned with this axis are absorbed by the mechanical structure. This results in a broader distribution of impulse values in the y-direction in Fig. 2. Despite these variations, Fig. 2(b) shows that most data points remain within two standard deviations, indicating a normal distribution of impulse values. This data distribution suggests that most the measured impulses follow a consistent trend, aligning with the regression line. The slope of the regression line represents the energy-to-impulse ratio, calculated as 3 μN s/J. Another notable observation is that if the regression line were extrapolated to 0 J input energy, it would predict an impulse of 156 μN s, which is unrealistic. At energy levels below 4 J, the input energy and impulse output are not necessarily linearly correlated. This scenario below 4J suggests that applying a linear regression model to predict impulse at zero energy input is not meaningful.

Fig. 24(b) shows that most data points lie within two standard deviations of the regression line, indicating that the regression model accurately represents the measurement data. Given that the actual data is expected to fall within ±29.83 % of the measured values, as shown in Fig. 24(a), the exact values will be within the region bounded by the two dashed lines. For an input energy of 5 J, the expected measured value from the regression line is 171 μN s, while the actual value, due to measurement error, is expected to range from 120 μN s to 222 μN s. The maximum actual impulse, 222 μN s, is significantly lower than the ideal impulse of 340 μN s. However, the minimum actual impulse, 120 μN s, still exceeds that of most 5 J input energy pulsed plasma thrusters. Future measurements of long-duration fuel ablation rates will be necessary to further analyze the impulse-to-fuel ratio and energy efficiency, providing a more straightforward assessment of the thruster's actual performance.

4. Conclusion

In this study, we developed and calibrated a hanging pendulum thrust stand designed for impulse measurements of PPT. The thrust stand had an ESC calibration system, an eddy current damping mechanism, and a high-precision laser displacement sensor to achieve accurate and repeatable impulse measurements.

During calibration, we identified key factors affecting measurement accuracy, including the influence of cable-induced parasitic stiffness and damping. These effects led to variations in the system's effective spring constant and damping coefficient, contributing to deviations in impulse measurements. By performing Fourier transform analysis on the thrust stand's response signal, we confirmed that shifts in damped oscillation frequency were responsible for inconsistencies inspecific calibration data points.

Uncertainty analysis revealed that the most significant contributor to impulse measurement error (30 %) originated from ESC pulse width variations due to power supply response delays. Additionally, parasitic mechanical effects from the electrical wiring introduced further uncertainties, highlighting the need for improved cable management and isolation strategies.

Experimental results demonstrated that the measured impulse output of the PPT correlated well with energy input within the 4 J–20 J range. The fitted line for the input energy range of 4 J–20 J can be used to represent the measured values. However, the actual impulse will fall within ±29.83 % of the measured values due to measurement errors from the thrust stand. Therefore, the study estimates that the impulse at 5 J input energy will range between 120 and 222 μN s.

Future improvements to the thrust stand will focus on refining the ESC calibration system to minimize pulse width variations, optimizing cable routing to reduce parasitic mechanical effects, and investigating alternative calibration methods to enhance overall measurement accuracy. These advancements will further improve the reliability of impulse measurements for pulsed electric propulsion systems, contributing to the precise characterization and optimization of next-generation PPT designs.

CRediT authorship contribution statement

Yueh-Heng Li: Writing – review & editing, Supervision, Resources, Project administration, Investigation, Funding acquisition, Conceptualization. **Wai-Cheng Lien:** Validation, Software, Methodology, Investigation, Formal analysis, Data curation, Conceptualization. **Sheng-Wen Liu:** Writing – review & editing, Validation, Investigation, Formal analysis, Conceptualization.

Declaration of competing interest

All authors declared that: (i) no support, financial or otherwise, has been received from any organization that may have an interest in the submitted work; and (ii) there are no other relationships or activities that could appear to have influenced the submitted work.

Acknowledgment

This study was financially supported by the National Science and Technology Council under Grant Nos. NSTC 112-2628-E-006-005-MY3, NSTC 113-2223-E-006-010, and NSTC 113-2218-E-006-020.

References

[1] J.E. Polk, A. Pancotti, T. Haag, S. King, M. Walker, J. Blakely, J. Ziemer, Recommended practice for thrust measurement in electric propulsion testing, J. Propul. Power 33 (2017) 539–555.
[2] A. Iwakawa, S. Mizojiri, Hall-effect thruster system of fully water propellant with microwave discharge cathode, Acta Astronaut. 232 (2025) 307–315.
[3] Y.-H. Li, T.-Y. Huang, M.M. Shen, Y.-C. Chen, Development of miniature radio frequency ion thruster with inductively coupled plasma source, J. Aeronaut. Astronaut. Aviat. 55 (2023) 13–28.
[4] A.A. Shagayda, D.A. Kravchenko, M.Y. Selivanov, D. Tomilim, Near-wall conductivity of primary electrons in the discharge chamber of an ion thruster, J. Aeronaut. Astronaut. Aviat. 56 (2024) 603–614.
[5] D.A. Kravchenko, A.A. Shagayda, M.Y. Selivanov, A.S. Lovtsov, Comparative numerical research of plasmas in ion thruster discharge chambers with different magnetic system types, J. Aeronaut. Astronaut. Aviat. 55 (2023) 535–543.
[6] Y.-H. Li, S. Palagiri, P.-Y. Chang, C. Montag, G. Herdrich, Plasma behavior in a solid-fed pulsed plasma thruster, J. Aeronaut. Astronaut. Aviat 51 (2019) 31–42.
[7] C.-W. Huang, P.-H. Huang, Z.-Y. Yang, Y.-H. Li, A study on iron-composite polymer propellants for improved plasma generation in electric propulsion systems, Chem. Eng. J. 508 (2025) 160990.
[8] Y.-H. Li, K. Dorn, H.-C. Hsieh, T.-C. Kuo, Y.-C. Hsu, Effect of electrode angle on pulsed plasmathruster performance, J. Aeronaut. Astronaut. Aviat. 53 (2021) 353–368.
[9] Y.-H. Li, C. Royer, Effect of voltage on second-stage electrodes of dual-stage solid propellant pulsed plasma thruster, Vacuum 167 (2019) 103–112.
[10] Y.-H. Li, J.-Y. Pan, G. Herdrich, Design and demonstration of micro-scale vacuum cathode arc thruster with inductive energy storage circuit, Acta Astronaut. 172 (2020) 33–46.
[11] O. Yang, L. Yuqi, Z. Yu, W. Jianjun, C. Yuqiang, Impulse measurement methods for space micro-propulsion systems, in: L. Dr Longbiao (Ed.), Propulsion Systems - Recent Advances, New Perspectives and Applications, IntechOpen, Rijeka, 2023. Ch. 5.
[12] D. Tsifakis, Development of Cubesat Thrusters, 2022.
[13] S.A. Popov, E.L. Dubrovskaya, A.V. Schneider, A.V. Batrakov, Measurement of momentum and recoil impulse of plasma jet of vacuum arc thruster, IEEE Trans. Plasma Sci. 49 (2021) 2567–2574.
[14] D.H. Lewis Jr., S.W. Janson, R.B. Cohen, E.K. Antonsson, Digital micropropulsion, Sensor Actuator Phys. 80 (2000) 143–154.
[15] Y.-K. Chang, S.-J. Kang, H.-R. Cho, Development of a Micro-thruster Impulse Measurement System Using Optical Sensors, 2008.
[16] Y. Ou, Y. Zhang, J. Wu, S. Tan, X. Du, Measurement method by inferring the thrust from the stress of the cantilever beam based on the photoelasticity theory, Appl. Opt. 58 (2019) 9746–9749.
[17] R.J. Radley, A Performance Study of a Pulsed Solid Fuel Microthruster, Massachusetts Institute of Technology, 1969.
[18] C. Zhu, M. Zhao, H. Zhang, Y. Yang, Y. Zheng, Study on thruster thrust measurement based on parallelogram mechanism, Chin. J. Sci. Instrum. 43 (2022) 98–107.
[19] A.R. Wong, A. Toftul, K.A. Polzin, J.B. Pearson, Non-contact thrust stand calibration method for repetitively pulsed electric thrusters, Rev. Sci. Instrum. 83 (2012).
[20] M.J. Wilson, S.S. Bushman, R. Burton, A compact thrust stand for pulsed plasma thrusters, IEPC Paper (1997).
[21] M.S. Glascock, J.L. Rovey, K.A. Polzin, Impulse and performance measurements of electric solid propellant in a laboratory electrothermal ablation-fed pulsed plasma thruster, Aerospace 7 (2020) 70.
[22] T.W. Haag, Thrust stand for pulsed plasma thrusters, Rev. Sci. Instrum. 68 (1997) 2060–2067.
[23] D.L.O. Soares, R.I. Marques, In vacuum dynamic and static tests of a thrust balance for electric propulsion with hysteresis analysis and behaviour prediction with transfer function, Meas. Sci. Technol. 32 (2021) 125903.
[24] Y.-X. Yang, L.-C. Tu, S.-Q. Yang, J. Luo, A torsion balance for impulse and thrust measurements of micro-Newton thrusters, Rev. Sci. Instrum. 83 (2012) 015105.
[25] S. Ciaralli, M. Coletti, S.B. Gabriel, An impulsive thrust balance for applications of micro-pulsed plasma thrusters, Meas. Sci. Technol. 24 (2013) 115003.
[26] M.R. Anselmo, R.I. Marques, Torsional thrust balance for electric propulsion application with electrostatic calibration device, Meas. Sci. Technol. 30 (2019) 055903.
[27] A.J. Jamison, A.D. Ketsdever, E. Muntz, Gas dynamic calibration of a nano-Newton thrust stand, Rev. Sci. Instrum. 73 (2002) 3629–3637.
[28] N.P. Selden, A.D. Ketsdever, Comparison of force balance calibration techniques for the nano-Newton range, Rev. Sci. Instrum. 74 (2003) 5249–5254.
[29] J.K. Ziemer, Performance measurements using a sub-micronewton resolution thrust stand, in: 27th International Electric Propulsion Conference, 2001.

[30] A.P. Pancotti, M.S. Hilario, M. Gilpin, E. Research, C.I.E.A. Ca, Comparison of Electrostatic Fins with Piezoelectric Impact Hammer Techniques to Extend Impulse Calibration Range of a Torsional Thrust Stand (Preprint), 2011.
[31] T.C. Lilly, A. Ketsdever, A.P. Pancotti, M. Young, Development of a specific impulse balance for capillary discharge pulsed plasma thrusters, J. Propul. Power 25 (2009) 823–826.
[32] J.H. Hsieh, P.-H. Huang, Y.-L. Huang, H. Juwantono, Y.-H. Li, Analysis of anode surface roughness influence on heaterless hollow cathode discharge, Phys. Scripta 99 (2024) 035607.
[33] J.H. Hsieh, Y.-L. Huang, P.-H. Huang, Y.-H. Li, Investigation of anode diameter and keeper geometry influence on open-end emitter heaterless hollow cathode discharge, Vacuum 229 (2024) 113504.
[34] Y.-L. Huang, J.H. Hsieh, W.-C. Wang, Y.-H. Li, Investigation of discharge voltage characteristics of a lanthanum hexaboride heaterless hollow cathode, Acta Astronaut. 226 (2025) 760–771.
[35] Y.-H. Li, Y.-C. Chen, S.-W. Liu, A.R. Aslan, Prediction and optimization of thrust performance from plasma diagnostics in the inductively coupled plasma of an RF ion thruster, Acta Astronaut. 208 (2023) 130–141.
[36] J.H. Hsieh, Y.-H. Li, Review of hollow cathode discharge: exploring advanced design and optimization, J. Aeronaut. Astrinaut. Aviat. 55 (2023) 385–414.
[37] J.H. Hsieh, M.M. Shen, Y.-H. Li, P.-H. Huang, Development of a lanthanum hexaboride hollow cathode for a magnetic octupole thruster, Vacuum 214 (2023) 112146.
[38] W.A. Johnson, L.K. Warne, Electrophysics of micromechanical comb actuators, J. Microelectromech. Syst. 4 (1995) 49–59.
[39] A. Yan, B. Appel, J. Gedrimas, MilliNewton thrust stand calibration using electrostatic fins, in: 47th AIAA Aerospace Sciences Meeting Including the New Horizons Forum and Aerospace Exposition, 2009, p. 212.
[40] R.L. Burton, Pulsed plasma thruster performance for microspacecraft propulsion, Micropropulsion for Small Spacecraft, Prog. Astronaut. Aeronaut. 187 (2000) 337–352.
[41] S. Bushman, R. Burton, E. Antonsen, Arc measurements and performance characteristics of a coaxial pulsed plasma thruster, in: 34th AIAA/ASME/SAE/ASEE Joint Propulsion Conference and Exhibit, 1998, p. 3660.
[42] S. Jaeger, R. Burton, J. Laystrom, G. Benavides, Optimization of performance and efficiency of a coaxial pulsed plasma thruster, in: 38th AIAA/ASME/SAE/ASEE Joint Propulsion Conference & Exhibit, 2002, p. 3977.
[43] H.A. Sodano, J.-S. Bae, D.J. Inman, W. Keith Belvin, Concept and model of eddy current damper for vibration suppression of a beam, J. Sound Vib. 288 (2005) 1177–1196.
[44] E.R. Cohen, An introduction to error analysis: the study of uncertainties in physical measurements, Meas. Sci. Technol. 9 (1998) 22.
[45] W.A. Fuller, Measurement Error Models, John Wiley & Sons, 2009.
[46] M. Kößling, M. Tajmar, Design and performance of a nano-Newton torsion balance, Rev. Sci. Instrum. 93 (2022) 074502.